

See discussions, stats, and author profiles for this publication at: <https://www.researchgate.net/publication/233453524>

High-Reynolds number Rayleigh–Taylor turbulence

Article in *Journal of Turbulence* · January 2009

DOI: 10.1080/14685240902870448

CITATIONS

79

READS

139

6 authors, including:



Daniel Livescu

Los Alamos National Laboratory

141 PUBLICATIONS 1,662 CITATIONS

[SEE PROFILE](#)



Andrew W. Cook

Lawrence Livermore National Laboratory

65 PUBLICATIONS 2,509 CITATIONS

[SEE PROFILE](#)

Some of the authors of this publication are also working on these related projects:



Simulating non-Gaussian scalar turbulent fields using a reaction analogy based method [View project](#)



Artificial Viscosity [View project](#)

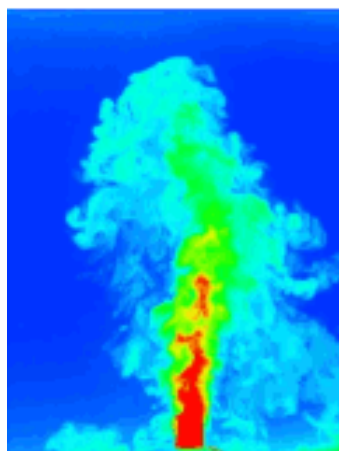
This article was downloaded by: [Los Alamos National Laboratory]

On: 7 July 2009

Access details: Access Details: [subscription number 908034759]

Publisher Taylor & Francis

Informa Ltd Registered in England and Wales Registered Number: 1072954 Registered office: Mortimer House, 37-41 Mortimer Street, London W1T 3JH, UK



Journal of Turbulence

Publication details, including instructions for authors and subscription information:

<http://www.informaworld.com/smpp/title~content=t713665472>

High-Reynolds number Rayleigh-Taylor turbulence

D. Livescu^a; J. R. Ristorcelli^a; R. A. Gore^a; S. H. Dean^a; W. H. Cabot^b; A. W. Cook^b

^a Los Alamos National Laboratory, Los Alamos, NM, USA ^b Lawrence Livermore National Laboratory, Livermore, CA, USA

First Published on: 01 January 2009

To cite this Article Livescu, D., Ristorcelli, J. R., Gore, R. A., Dean, S. H., Cabot, W. H. and Cook, A. W. (2009) 'High-Reynolds number Rayleigh-Taylor turbulence', Journal of Turbulence, Volume 10, Art. No. N13,

To link to this Article: DOI: 10.1080/14685240902870448

URL: <http://dx.doi.org/10.1080/14685240902870448>

PLEASE SCROLL DOWN FOR ARTICLE

Full terms and conditions of use: <http://www.informaworld.com/terms-and-conditions-of-access.pdf>

This article may be used for research, teaching and private study purposes. Any substantial or systematic reproduction, re-distribution, re-selling, loan or sub-licensing, systematic supply or distribution in any form to anyone is expressly forbidden.

The publisher does not give any warranty express or implied or make any representation that the contents will be complete or accurate or up to date. The accuracy of any instructions, formulae and drug doses should be independently verified with primary sources. The publisher shall not be liable for any loss, actions, claims, proceedings, demand or costs or damages whatsoever or howsoever caused arising directly or indirectly in connection with or arising out of the use of this material.

High-Reynolds number Rayleigh–Taylor turbulence

D. Livescu^{a,*}, J.R. Ristorcelli^a, R.A. Gore^a, S.H. Dean^a, W.H. Cabot^b and A.W. Cook^b

^aLos Alamos National Laboratory, Los Alamos, NM 87544, USA; ^bLawrence Livermore National Laboratory, Livermore, CA 94550, USA

(Received 14 July 2008; final version received 11 December 2008)

The turbulence generated in the variable density Rayleigh–Taylor mixing layer is studied using the high-Reynolds number fully resolved 3072³ numerical simulation of Cabot and Cook (Nature Phys. 2 (2006), pp. 562–568). The simulation achieves bulk Reynolds number, $Re = \frac{H\dot{H}}{\nu} = 32,000$, turbulent Reynolds number, $Re_t = \frac{\bar{k}^2}{\nu\varepsilon} = 4600$, and Taylor Reynolds number, $R_\lambda = 170$. The Atwood number, A , is 0.5, and the Schmidt number, Sc , is 1. Typical density fluctuations, while modest, being one quarter the mean density, lead to non-Boussinesq effects. A comprehensive study of the variable density energy budgets for the kinetic energy, mass flux and density specific volume covariance equations is undertaken. Various asymmetries in the mixing layer, not seen in the Boussinesq case, are identified and explained. Hypotheses for the variable density turbulent transport necessary to close the second moment equations are studied. It is found that, even though the layer width becomes temporally self-similar relatively fast, the transient effects in the energy spectrum remain important for the duration of the simulation. Thus, the dissipation does not track the spectral energy cascade rate and the integral lengthscale does not follow the expected Kolmogorov scaling, $\bar{k}^{3/2}/\varepsilon$. As a result, the popular eddy diffusivity expression, $\nu_t \sim \bar{k}^2/\varepsilon$, does not model the temporal variation of the turbulent transport in any of the moment equations. An eddy diffusivity based on a lengthscale related to the layer width is found to work well in a gradient transport hypothesis for the turbulent transport; however, that lengthscale is a global quantity and does not lead to pointwise, local closure. Therefore, although the transient effects may vanish asymptotically, it is suggested that, even long after the onset of the self-similar growth, two separate lengthscale equations (or equivalent) are needed in a moment closure strategy for Rayleigh–Taylor turbulence: one for the turbulent transport and the other for the dissipation. Despite the fact that the intermediate scales are nearly isotropic, the small scales have a persistent anisotropy; this is due to a cancellation between the viscous and nonlinear effects, so that the anisotropic buoyancy production remains important at the smallest scales.

Keywords: Rayleigh–Taylor instability; DNS; variable density turbulence; turbulent mixing; moment closure; anisotropy

1. Introduction

Molecular mixing as a consequence of stirring by fluid motion is an important process in many practical applications. If the microscopic densities of the fluids participating in the mixing are very different, we refer to such flows as variable density (VD) flows in contrast to the Boussinesq approximation in which the densities are close. In such

*Corresponding author. Email: livescu@lanl.gov

a flow, due to the tight coupling between the density and the velocity field, in addition to the quadratic nonlinearities of the incompressible Navier–Stokes equations, new cubic nonlinearities arise. In addition, in a VD fluid, the velocity field is no longer solenoidal and the specific volume, a function of the amount of each material present, is a new dependent variable. VD mixing is encountered in atmospheric and ocean flows, astrophysical flows, combustion, and many flows of chemical engineering interest. In a VD flow, the mixing process becomes fundamentally different than for the Boussinesq case [2]. Many of these flows are driven by acceleration (e.g., gravity in geophysical and astrophysical flows) which, because the density is not uniform, leads to large differential fluid accelerations. If the acceleration is constant and the fluid configuration is unstable (i.e., the density gradient points opposite to the body force), a fluid instability is generated in which perturbations of the initial interface between the fluids can grow, interact nonlinearly, and lead to turbulence. This instability is known as the Rayleigh–Taylor (RT) instability and is of fundamental importance in a multitude of applications, from fluidized beds, oceans and atmosphere, to ICF and supernovae explosions.

Here, we consider a variable density flow with two different density fluids, such that the macroscopic specific volume is related to the mass fractions of the two fluids by

$$v^* = \frac{1}{\rho^*} = \frac{Y_1}{\rho_1} + \frac{Y_2}{\rho_2}, \quad (1)$$

where $Y_1 + Y_2 = 1$ and ρ_1 and ρ_2 are the “microscopic densities” of the two pure fluids and are constant for incompressible fluids. The index “2” refers to the heavier fluid. The mixture density ρ^* and the specific volume, v^* , change in both space and time. Such a flow model describes active mixing in low speed flows, in which the turbulent Mach number is small and the fluids participating in the mixing have constant microscopic densities.

The primary nondimensional parameter characterizing the differential acceleration effects is the Atwood number:

$$A \equiv \frac{\rho_2 - \rho_1}{\rho_2 + \rho_1} \quad \Rightarrow \quad \frac{\rho_2}{\rho_1} = \frac{1 + A}{1 - A}. \quad (2)$$

We examine the variable density mixing and turbulence in the highest Reynolds number fully resolved simulation to date, performed by Cabot and Cook [1]. This simulation and those of [2, 3] represent the only fully resolved simulations (we believe) of developed variable density turbulence at Atwood numbers, while relatively modest at $A = 0.5$, large enough to generate non-Boussinesq, VD effects. While the results are obtained from fully resolved simulations, our investigation and discussion of the flow is guided by the first and second Favre moment equations [4, 5]. This is useful from two points of view: (1) it allows one to understand what the flow is doing “on average” to better diagnose any new physics and (2) it provides data and information useful to low-dimensional turbulence models.

The study addresses several issues relevant to variable density turbulence:

- (1) A detailed examination of the energy budgets of the Favre-averaged kinetic energy, mass flux and density specific volume correlation transport equations.
- (2) The applicability of the simple and ever popular diffusive engineering “gradient transport” models for the mass weighted advective turbulent transport. Specifically, models for the mass weighted turbulent transport of the Favre-averaged kinetic energy, mass flux and density specific volume correlation.

- (3) The differences with the Boussinesq case, as reflected in the asymmetry of various quantities.
- (4) The effects of buoyancy on VD turbulence at all scales of the motion and the universality of the small scales.
- (5) Providing data for second-order moment closures development, validation and verification.

Section 2 summarizes the mathematical statement of the problem. The instantaneous and the Favre-averaged equations for the first and second moments, that guide our diagnosis, are given. In Section 3, the large scale quantities characterizing the mixing layer and its asymmetries, underlying the non-Boussinesq aspects of the flow, are discussed. Subsequently, in Section 4, the energy budgets for the Favre kinetic energy, mass flux and density specific volume covariance are undertaken. Modeling issues related to the gradient transport hypothesis are then outlined. The summary and conclusions follow. An appendix is devoted to the comparison of this inhomogeneous Rayleigh–Taylor simulation to, what we call, the homogeneous Rayleigh–Taylor (HRT) simulations of [2, 3]. In general, all the conclusions from these less-expensive simulations are relevant and borne out by the current single RT realization.

2. Governing equations

The mathematical model describing the mixing of two incompressible fluids with different densities subject to a constant acceleration is provided by the Navier–Stokes equations and species mass fraction transport equations [1, 6, 7]:

$$(\rho^* u_i^*),_t + (\rho^* u_i^* u_j^*),_j = -p^*_{,i} + \tau_{ij}^* + \rho^* g_i \quad (3)$$

$$(\rho^* Y_m^*),_t + (\rho^* Y_m^* u_j^*),_j = \mathcal{D}(\rho^* Y_{m,j}^*),_j \quad (4)$$

where $*$ denotes total (instantaneous) variables. The viscous stress is considered Newtonian with

$$\tau_{ij}^* = \mu \left[u_{i,j}^* + u_{j,i}^* - \frac{2}{3} u_{k,k}^* \delta_{ij} \right] = \mu S_{ij}^* \quad (5)$$

and the mass diffusion Fickian, with constant diffusion coefficient, \mathcal{D} .

In Equations (3) and (4), u_i^* is the velocity in direction i , ρ^* is the mixture density, p^* is the pressure, Y_m^* is fluid m mass fraction and $g_i = (0, 0, -g)$ is the (constant) acceleration in direction i . The independent variables are the time, t , and space variables, x_i . The kinematic viscosity, $\nu = \mu/\rho^*$, and the Schmidt number, $Sc = \nu/\mathcal{D}$, are assumed constant. Thus, the stress tensor can be written as $\tau_{ij}^* = \nu \rho^* S_{ij}^*$. Note that, in general, the dynamic viscosity, μ , is a weaker function of density; the assumption ν constant ensures a uniform Sc throughout the flow.

Summing over $m = 1, 2$ in the mass fraction equation and using $Y_1^* + Y_2^* = 1$ leads to the continuity and, equivalently, the specific volume, $v^* = 1/\rho^*$, equations:

$$\rho^*_{,t} + (\rho^* u_j^*),_j = 0 \quad (6)$$

$$v^*_{,t} + (v^* u_j^*),_j = 2v^* u_{k,k}^*. \quad (7)$$

The change in the specific volume during mixing leads to nonzero divergence of velocity. For Fickian diffusion, the divergence is [6]

$$u_{j,j}^* = -\mathcal{D}(\ln \rho^*)_{,jj}. \quad (8)$$

2.1. The moment equations

In this section, the general first and second moment equations for a buoyancy-driven variable density fluid are given. As the flow is periodic in the horizontal directions, the moments are planar averages taken perpendicular to the direction of gravity and parallel to the initial mean interface. The equations are first presented in a general form, without making use of (8), so that they are formally the same for a fully compressible, multi-component flow.

In defining the turbulence quantities, capital roman letters, overbars, and angle brackets are used to denote Reynolds averages. Angle brackets are preferred for longer expressions while overbars are used for quantities named with Greek letters. Lower case letters (Roman or Greek) or primes are used to denote fluctuations. As the density is not spatially uniform, some of the results are presented using density weighted (Favre) averages, denoted with $\tilde{\cdot}$, and the corresponding fluctuations with double primes. Thus, the instantaneous velocity, density, pressure, and specific volume are decomposed as $u_i^* = U_i + u_i = \tilde{U}_i + u_i''$, $\rho^* = \bar{\rho} + \rho$, $p^* = P + p$, and $v^* = V + v$, respectively. Note that $\tilde{U}_i - U_i = u_i - u_i'' = a_i$. The definitions for the normalized mass flux, a_i , Favre Reynolds stresses, R_{ij} , turbulent kinetic energy, \tilde{k} , and total kinetic energy, E_K , and mass fraction flux, Υ_{m_j} , are given below:

$$a_i = \frac{\langle u_i \rho \rangle}{\bar{\rho}} = -\langle u_i'' \rangle, \quad (9)$$

$$R_{ij} = \langle \rho^* u_i'' u_j'' \rangle = \bar{\rho} \langle u_i u_j \rangle - \bar{\rho} a_i a_j + \langle \rho u_i u_j \rangle, \quad (10)$$

$$\tilde{k} = R_{kk}/(2\bar{\rho}) = (\langle u_i u_i \rangle - a_i a_i + \langle \rho u_i u_i \rangle / \bar{\rho})/2, \quad (11)$$

$$E_K = \langle \rho^* u_i^* u_i^* \rangle / 2 = (\bar{\rho} \langle u_i u_i \rangle + \langle \rho u_i u_i \rangle) / 2, \quad (12)$$

$$\Upsilon_{m_j} = \langle \rho^* u_j'' Y_m'' \rangle. \quad (13)$$

The Favre first moment (or mean) equations are written as:

$$\frac{\partial}{\partial t} \bar{\rho} + (\bar{\rho} \tilde{U}_j)_{,j} = 0 \quad (14)$$

$$\frac{\partial}{\partial t} (\bar{\rho} \tilde{U}_i) + [\bar{\rho} \tilde{U}_i \tilde{U}_j]_{,j} + R_{ij,j} = -P_{,i} + \bar{\tau}_{ij,j} + \bar{\rho} g_i \quad (15)$$

$$\frac{\partial}{\partial t} (\bar{\rho} \tilde{Y}_m) + [\bar{\rho} \tilde{Y}_m \tilde{U}_j]_{,j} + \Upsilon_{m_j} = \mathcal{D}(\bar{\rho} \tilde{Y}_{m,j})_{,j} + \mathcal{D}(\rho^* Y_{m,j}'')_{,j} \quad (16)$$

$$\tilde{U}_{j,j} - a_{j,j} = -\mathcal{D} \left\langle \frac{\rho_{,j}^*}{\rho^*} \right\rangle_{,j} \quad (17)$$

Equations (14)–(16) are formally the same for a fully compressible flow. For incompressible two-fluid mixing, the mean density (14) and mean mass fraction equations (16) are not independent; we will retain the mean density equation and consider the mean mass fraction equations only for completeness.

The equations for the Reynolds stresses and normalized mass flux, which are unclosed in Equation (15), can be written following [4] as

$$\frac{\partial}{\partial t} R_{ij} + (\tilde{U}_l R_{ij})_{,l} + R_{ijl,l} = P_{ij} + \Pi_{ij} - \varepsilon_{ij} - T_{ijl,l}, \quad (18)$$

$$\begin{aligned} \frac{\partial}{\partial t} (\bar{\rho} a_i) + (\bar{\rho} \tilde{U}_j a_i)_{,j} &= -\langle \rho v \rangle P_i + \bar{\rho} \langle v p_i \rangle - \bar{\rho} a_j (\tilde{U}_i - a_i)_{,j} \\ &+ \frac{\bar{\rho}_{,j}}{\bar{\rho}} (\langle \rho u_i u_j \rangle - R_{ij}) + \bar{\rho} (a_i a_j)_{,j} \\ &- (\langle \rho u_i u_j \rangle_{,j} + \bar{\rho} \langle u_i d \rangle). \end{aligned} \quad (19)$$

The production term, P_{ij} , appears with the opposite sign in the equations for $\tilde{U}_k \tilde{U}_k$; it represents a transfer of turbulence to and from the mean Favre energy. The definitions of the terms on the right-hand side of the R_{ij} equation are

$$P_{ij} = -R_{il} \tilde{U}_{j,l} - R_{jl} \tilde{U}_{i,l} + a_i P_j + a_j P_i, \quad (20)$$

$$T_{ijl} = \langle p u_j \rangle \delta_{il} + \langle p u_i \rangle \delta_{jl} - \langle u_j \tau_{il} + u_i \tau_{jl} \rangle, \quad (21)$$

$$R_{ijl} = \langle \rho^* u_i'' u_j'' u_l'' \rangle, \quad (22)$$

$$P_i = P_{,i} - \bar{\tau}_{ij,j}, \quad (23)$$

$$\Pi_{ij} = \langle p(u_{i,j} + u_{j,i}) \rangle, \quad (24)$$

$$\varepsilon_{ij} = \langle \tau_{il} u_{j,l} + \tau_{jl} u_{i,l} \rangle. \quad (25)$$

The quantity $b = -\langle \rho v \rangle$ is a measure of the mixing state and is unclosed in the production term for the normalized mass flux in 19. The transport equation for b is typically written as

$$\frac{\partial}{\partial t} b + U_j b_{,j} = -\frac{1+b}{\bar{\rho}} (\bar{\rho} a_j)_{,j} - \bar{\rho} \langle v u_j \rangle_{,j} + 2\bar{\rho} \langle v d \rangle. \quad (26)$$

More intuitively, one can write an equation for the mean specific volume:

$$\frac{\partial}{\partial t} V + (U_j V)_{,j} = 2VD - \langle u_j v \rangle_{,j} + 2\langle v d \rangle, \quad (27)$$

where $d = u_{i,i}$ and $D = U_{i,i}$. For variable density turbulence, using $\rho^* v^* = 1$, the following identities follow:

$$1 = \bar{\rho} V + \rho V + \bar{\rho} v + \rho v, \quad (28)$$

$$\bar{\rho} V = 1 - \langle \rho v \rangle = 1 + b, \quad (29)$$

$$\bar{\rho} \langle u_i v \rangle = -\langle u_i \rho \rangle V - \langle u_i \rho v \rangle = -a_i \bar{\rho} V - \langle u_i \rho v \rangle. \quad (30)$$

The last equation is obtained by taking the moment with u_i of the first and re-arranging; it is exact. Thus, a closure for the volume flux is given in terms of the normalized mass flux provided an expression for the triple moment can be found.

A moment closure approach at the second-order level requires modeled transport equations for the Favre turbulent kinetic energy, \tilde{k} , normalized mass flux, a_i , and density specific

volume correlation, b , or, alternatively, mean specific volume, V . Using the relations above, the corresponding transport equations are written as

$$\begin{aligned} \frac{\partial}{\partial t} \bar{\rho} \tilde{k} + (\bar{\rho} \tilde{U}_j \tilde{k})_{,j} &= a_i (P_{,i} - \bar{\tau}_{ij,j}) - R_{ij} \tilde{U}_{i,j} - \frac{1}{2} R_{ii,j,j} \\ &\quad - \langle u_i (p \delta_{ij} - \tau_{ij}) \rangle_{,j} + \langle p d \rangle - \langle \tau_{ij} u_{i,j} \rangle, \end{aligned} \quad (31)$$

$$\begin{aligned} \frac{\partial}{\partial t} (\bar{\rho} a_i) + (\bar{\rho} \tilde{U}_k a_i)_{,k} &= b P_i + \bar{\rho} \langle v p_i \rangle - \bar{\rho} a_j (\tilde{u}_i - a_i)_{,j} + \frac{\bar{\rho}_{,j}}{\bar{\rho}} (\langle \rho u_i u_j \rangle - R_{ij}) \\ &\quad + \bar{\rho} (a_i a_j)_{,j} - (\langle \rho u_i u_j \rangle)_{,j} + \bar{\rho} \langle u_i d \rangle, \end{aligned} \quad (32)$$

$$\frac{\partial}{\partial t} b + \tilde{U}_j b_{,j} = 2a_j b_{,j} - 2a_j (1+b) \frac{\bar{\rho}_{,j}}{\bar{\rho}} + \bar{\rho} \left(\frac{\langle u_j \rho v \rangle}{\bar{\rho}} \right)_{,j} + 2\bar{\rho} \langle v d \rangle, \quad (33)$$

$$\frac{\partial}{\partial t} V + \tilde{U}_j V_{,j} = 2a_j V_{,j} + V \tilde{U}_{j,j} + \left(\frac{\langle u_j \rho v \rangle}{\bar{\rho}} \right)_{,j} + 2\langle v d \rangle. \quad (34)$$

The equations above are general and describe the moments' evolutions in a fully compressible flow, regardless of the equation of state. Only after the application of (8) they become specific to the VD case.

3. Investigating the basic flow physics

In this section, the turbulence properties inside the mixing layer are analyzed using metrics pertaining to buoyancy-driven turbulence: lengthscales, Reynolds numbers, normal stresses and their scale-dependent anisotropy, mean pressure gradient, density intensity, density specific volume correlation, turbulent kinetic energy, and potential energy conversion rate. The large scales of the flow, as characterized by various mixing layer widths and lengthscales, are shown to grow self-similarly. Various asymmetries inside the mixing layer, not seen in the Boussinesq case, are identified and explained.

3.1. RT self-similarity

The extent of the RT layer, and especially the rate of increase of the layer width, is an important question in applications and one metric to gauge the efficacy of various models and numerical simulations. It is generally agreed that (1) for domains large horizontally compared to any characteristic wavelength of the perturbation, (2) for domains much longer in the vertical direction than the width of the layer, and (3) for an initial perturbation spectrum peaked near the most unstable linear mode, the turbulent mixing layer grows quadratically in time. The quadratic growth has been known for a long time as a dimensionally consistent result confirmed by experimental data [8–10]. More recently [11], using the moment equations, provided the first exact analytical derivation of the self-similar growth rate for the Boussinesq case. The expression, $h = \alpha Agt^2 + 2(\alpha Ag h_0)^{1/2} t + h_0$ has a quadratic term in time but also a linear term which is important at early times. Cabot and Cook [1] accounted for the linear term by calculating $\alpha = \frac{h^2}{4Ag h}$ and showed that α reaches its self-similar value faster than the previous studies suggested. The data also suggest that the Boussinesq result holds for the VD case, at least to $A = 0.5$. The value obtained for the simulation examined here is $\alpha \approx 0.02$. This value is lower than that obtained in most experiments [12, 13]. In general, the discrepancy between the numerical and experimental values of α is an

open question, although recent results suggest this may be due to differences in the initial conditions [14].

For the miscible case there is no unique way to define the width of the mixing layer. Cabot and Cook [1] used the formula $h = \int_{-\infty}^{\infty} X_P(\bar{\rho}) dz$, where $X_P(\bar{\rho})$ is the maximum product in a fast reaction analogy [1, 2]. Physically, h is the thickness of mixed fluid that would result if the two fluids are perfectly homogenized. h is less sensitive to statistical variability than the more usual width formula $H = z_{\max} - z_{\min}$ with z_{\max} and z_{\min} being the z locations where the mean density reaches some given values, usually within 1% or 5% of the pure fluid values. For example, $H_{0.01}$ is defined as the maximum vertical distance between the points where the mean density equals $\rho_1 + 0.01(\rho_2 - \rho_1)$ and $\rho_2 - 0.01(\rho_2 - \rho_1)$. Figure 1 shows the time variation of the 1% and 5% half-widths, $H_{0.01}/2$ and $H_{0.05}/2$ and the corresponding bubble and spike heights, normalized by h . The ratios become approximately constant in time, $H_{0.01}/h \approx 2.4h$ and $H_{0.05}/h \approx 1.9h$, after $t/\tau \approx 6$, which is the time when α reaches a constant value [1] and the flow becomes self-similar. In all figures, the numerical time is nondimensionalized by $\tau = \sqrt{l_0/(Ag)}$, where l_0 is the dominant initial wavelength of the perturbation and corresponds to the most unstable wavelength of the linear problem.

Figure 1 also indicates that both the bubble and spike heights grow self-similarly after $t/\tau \approx 6$ and the spike-to-bubble height ratio becomes a constant. The ratio is larger if the heights are calculated based on the 1% density level, showing that the two sides of the layer are more asymmetric toward the edges (see also below). The values obtained, $H_s/H_b \approx 1.4$ for the 1% density level and ≈ 1.15 for the 5% density level, are within the range of previously reported experimental and numerical values [12, 14]. Thus, even though the value of α is lower than what is usually obtained experimentally, the layer edges exhibit similar asymmetry.

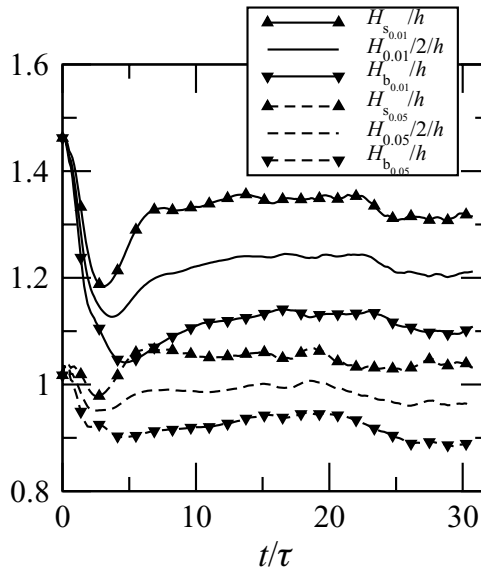


Figure 1. Time variation of the normalized 1% and 5% layer half-widths, and the corresponding bubble and spike heights.

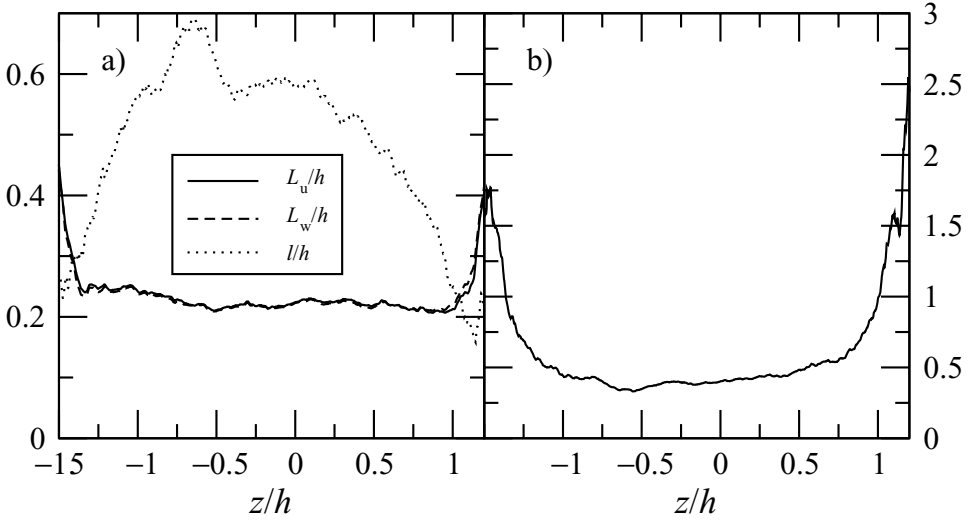


Figure 2. (a) Vertical variation of the integral lengthscales L_u , L_w , and $\ell = \tilde{k}^{3/2}/\varepsilon$ and (b) ratio L_w/ℓ , at $t/\tau = 31$.

As the mixing layer is turbulent at later times, the turbulence integral scale provides information about the size of the energy containing eddies in the layer. Figure 2(a) compares the integral scales, L_u and L_w , with h across the layer at the end of the simulation, when the Reynolds number is largest. L_u and L_w are calculated in the usual way from the 2D spectra [15]. L_u is based on the velocity u_i and L_w is based on the mass-weighted velocity $\sqrt{\rho^*/\bar{\rho}} u_i''$, to account for potential VD effects. The two lengthscales are about the same after the very early times, as the Favre turbulent kinetic energy \tilde{k} becomes close to the kinetic energy per unit mass $\langle u_i u_i \rangle / 2$, similar to [3]. The turbulence integral scale becomes almost constant across the layer for $-1.25h < z < h$.

Single-point turbulence models do not have access to the integral scale which requires spectral or two-point information. Such models usually assume the validity of Kolmogorov's zeroth law and use the turbulence scale $\ell = \tilde{k}^{3/2}/\varepsilon$, where $\varepsilon = \langle \tau_{ij} u_{i,j} \rangle$ is the dissipation of \tilde{k} (31), as a surrogate for the integral scale. Figure 2(a) shows that ℓ is not constant across the layer and peaks on the light fluid side. The values of L_w/ℓ in the central region of the layer vary between 0.3 and 0.5 close to those obtained in other high-Reynolds number flows [15]. At the edges, where the turbulent Reynolds number is small, Kolmogorov's zeroth law is not useful.

3.2. The turbulent Reynolds number

In RT turbulence, the range of flow scales increases continuously as the energy spectrum broadens at both ends. The bulk Reynolds number, $Re = \frac{H_{0.01} \dot{H}_{0.01}}{\nu}$, discussed in [1], is a measure of the large scales. The turbulent Reynolds number (Figure 3(a)), defined by $Re_t = \frac{\tilde{k}^2}{\nu \varepsilon}$, represents the magnitude of turbulent transport versus viscous transport and defines the width of the energy spectrum. From the point of view of single point closures, Re_t is an important quantity as the eddy viscosity is proportional to $\nu Re_t = \frac{\tilde{k}^2}{\varepsilon}$ in standard gradient transport models. At the end of the simulation $Re_{t_{\max}} \approx 4600$, corresponding to a

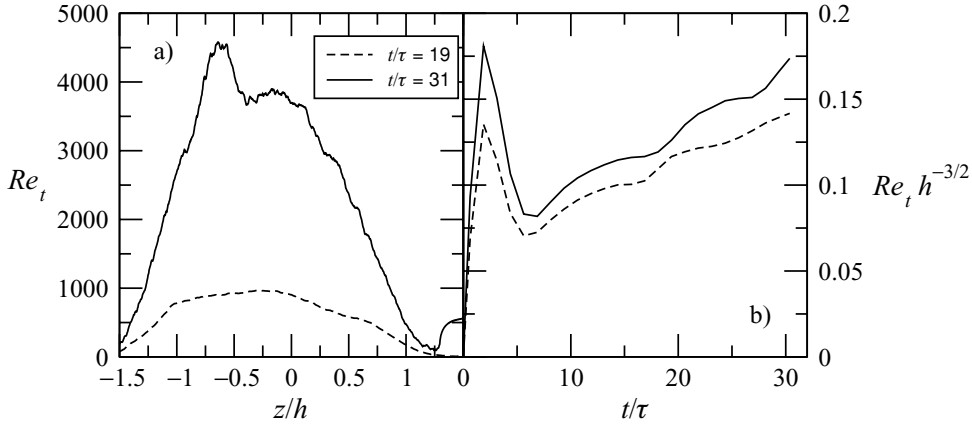


Figure 3. (a) Re_t across the layer in the turbulent regime. (b) Time variation of peak Re_t (continuous line) and Re_t at $z = 0$ multiplied by $h^{-1.5}$.

Taylor Reynolds number calculated using the isotropic formula $Re_\lambda = \sqrt{20/3 Re_t}$ of ≈ 175 . At the centerline, $Re_t \approx 3700$, corresponding to $Re_\lambda = 157$. Re_t peaks on the light fluid side, close to the turbulence scale l peak.

As the flow becomes self-similar, Re_t should grow, to leading order, as $\sim t^3$ [11]. Asymptotically, as the lower order terms in the self-similar relation become negligible, Re_t should grow as $h^{2/3}$. Figure 3(b) shows that neither the peak Re_t nor the centerline value follow this prediction. However, as shown below, the kinetic energy grows consistent with the Boussinesq self-similar analysis. It is concluded that the faster growth in Re_t compared to $h^{2/3}$ is due to the contributions from the lower order terms in the self-similar formulae for the kinetic energy and dissipation. Even after the onset of the self-similar growth, the spectral dynamics is still transient: there is a time lag between the rise in the large scales energy due to buoyancy production and when this increase is felt at the viscous scales. Thus, even though asymptotically Re_t may become proportional to $h^{2/3}$, the lack of asymptotic self-similarity (or proportionality to $h^{2/3}$) of Re_t throughout the simulation renders the gradient transport hypothesis for the transport terms using the usual turbulence eddy diffusivity, νRe_t , inappropriate (see also below).

3.3. Production over dissipation

The kinetic energy production to dissipation ratio, $\frac{P}{\varepsilon}$, where $P = a_i P_{,i}$ and $\varepsilon = \langle \tau_{ij} u_{i,j} \rangle$ (see Equations (31) and (42)), is shown in Figure 4. $\frac{P}{\varepsilon}$ is usually taken as a measure of the “non-equilibrium” nature of the flow. After the early times, production over dissipation varies slightly across the layer and peaks around the edges. At the centerline, $\frac{P}{\varepsilon}$ increases in time, following the general trend implied by the total kinetic energy over total production ($K/\delta P$) discussed in [1]. Thus, there is a time lag between the increase in energy at the large scales and the increase in the viscous dissipation.

This imbalance between production and dissipation suggests some phenomenological issues that relate to general “non-equilibrium” turbulent flows. These effects can be understood in the following way. Let the eddy cascade rate of \tilde{k} to smaller scales be ε_c . It is usual to parametrize the cascade rate following the notion of an efolding decrease of the energy on an eddy turnover timescale, $\tilde{k}^{1/2}/L$, accomplished by the energy cascade

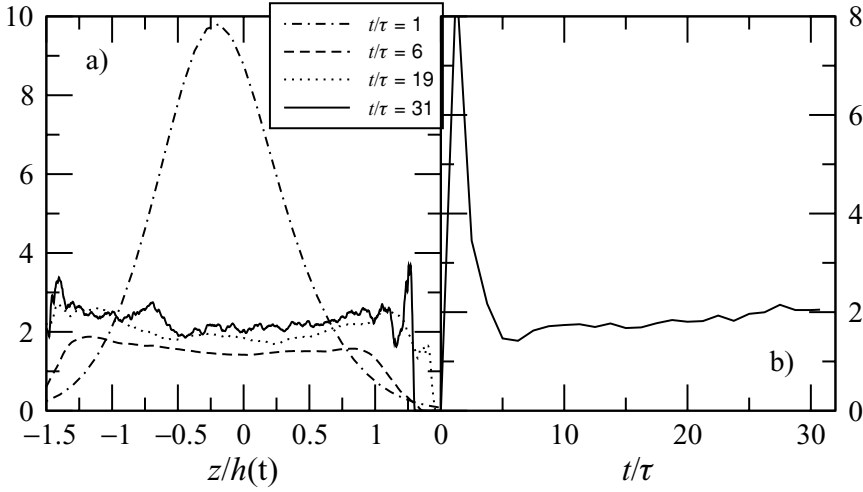


Figure 4. Energy production over dissipation, $\frac{P}{\epsilon}$, (a) across the layer and (b) at $z = 0$.

to smaller scales [16]. Here L is a quantity that is characteristic of the large scale features of the flow. In homogeneous isotropic turbulence, this scale is the two-point integral lengthscale.

If there is a change in the large scales kinetic energy due to a change in the production, geometry, etc., the finite time of the energy cascade process leads to a delay to the time such change is felt by the dissipation. Thus, in general, ϵ_c and ϵ are different (Figure 5(a)).

The cascade rate, ϵ_c , and the dissipation rate, ϵ , are, thus:

$$\epsilon_c = \tilde{k}^{3/2}/L, \quad \epsilon = \langle \tau_{ij} u_{i,j} \rangle. \quad (35)$$

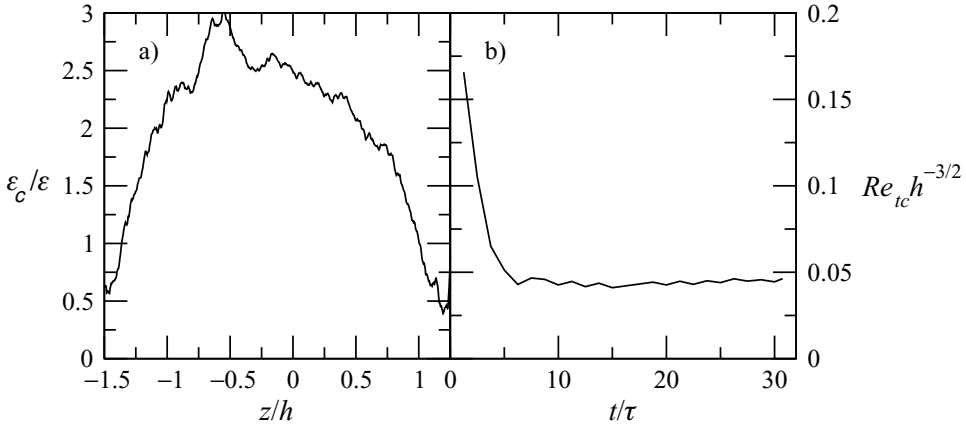


Figure 5. (a) Vertical variation of ϵ_c/ϵ at $t/\tau = 31$. (b) Time variation of $Re_{tc} = \tilde{k}^2/(\nu \epsilon_c)$ at the centerline. The integral scale used to calculate ϵ_c is $L = L_u$.

The first equality is phenomenological and the second a precise mathematical definition. At equilibrium, $\varepsilon_c = \varepsilon$, so that $L = \ell = \tilde{k}^{3/2}/\varepsilon$ and the turbulent Reynolds number becomes $Re_t = \bar{\rho} \tilde{k}^{1/2} \ell / \mu = \tilde{k}^2 / (\nu \varepsilon)$. Shown in Figure 5(b) is a Reynolds number based on $L = \tilde{k}^2 / \varepsilon_c$, $Re_{tc} = \tilde{k}^2 / (\nu \varepsilon_c)$, at the centerline, which is seen now to have the asymptotic self-similar scaling.

Several points follow from this discussion that are relevant to “non-equilibrium” flows and the turbulence modeling in such flows.

- (1) The lengthscale $\ell = \tilde{k}^{3/2}/\varepsilon$ does not characterize the large scales of the flow: $\ell \neq L$.
- (2) The lengthscale $\ell = \tilde{k}^{3/2}/\varepsilon$ does not characterize the large scales of the flow that are responsible for the turbulent transport and, as shown below, ℓ is not the relevant lengthscale for a gradient transport hypothesis.
- (3) The equilibrium notion that the viscous dissipation, responsible for the decrease of \tilde{k} , can be parametrized by the large scale relation $\tilde{k}^{3/2}/L$ is not tenable for “non-equilibrium” flows.

3.4. Non-Boussinesq effects

At low Atwood numbers, the mixing layer remains symmetrical around the centerline and the mean pressure equal to the hydrostatic pressure head. As the Atwood number is increased and the flow becomes non-Boussinesq, the bubble and spike sides start to differentiate, with the spikes falling faster than the ascending velocity of the bubbles [12]. In this section, differences compared to the Boussinesq case pertaining to (1) asymmetry of mixing layer, (2) density fluctuations, and (3) mean pressure gradient are investigated. The quantities examined are suggested by closures required for the moment equations.

3.4.1. Mean density profiles and mixing layer asymmetry

The mean density profile is linear in the innermost region of the RT layer. As the mixing layer grows, the profile expands at both ends but maintains a fixed point in the middle of the layer (Figure 6(a)). If z is scaled by the width of the layer h , then the density profiles collapse quite well after the initial time (Figure 6(b)). As $\bar{\rho}(z/h(t))$ remains the same in time, it yields that $z = 0$ is the fixed point in the density profile (for all other z values $\bar{\rho}(z)$ changes in time). The existence of a fixed point in the mean density profile located at $z = 0$ has important consequences for the asymmetry of various quantities, as detailed below.

The half-layer position, z_m , is an indication of the mixing layer asymmetry expected to become important at high A [12]. It is usually defined as the vertical position equally distanced from the edges of the layer. In this context the edges of the layer are the positions where the density reaches $n\%$ of the pure fluid densities, i.e., $\rho_1 + n/100(\rho_2 - \rho_1)$ and $\rho_2 - n/100(\rho_2 - \rho_1)$. z_m can also be defined from $\int_{-\infty}^{z_m} X_P(\bar{\rho}) dz = h/2$, in which case the notation z_{m_P} is used. Figure 7 shows $z_{m_{0.01}}$, $z_{m_{0.05}}$, and z_{m_P} . Interestingly, z_{m_P} coincides with the mean density profile fixed point and remains at $z = 0$. As most of the contribution to h comes from the interior of the layer, this suggests that the mixing layer, as reflected by the mean density, remains symmetrical with respect to the centerline in the central region. The half-layer positions based on the 0.01 and 0.05 density levels move toward the light fluid side, as the spikes penetrate more than the bubbles. After the very early times, z_m starts scaling with h . The mixing layer becomes more asymmetric at the edges as the bubble and spike fronts start moving with different velocities; $z_{m_{0.01}}$ moves more to the light fluid side than $z_{m_{0.05}}$.

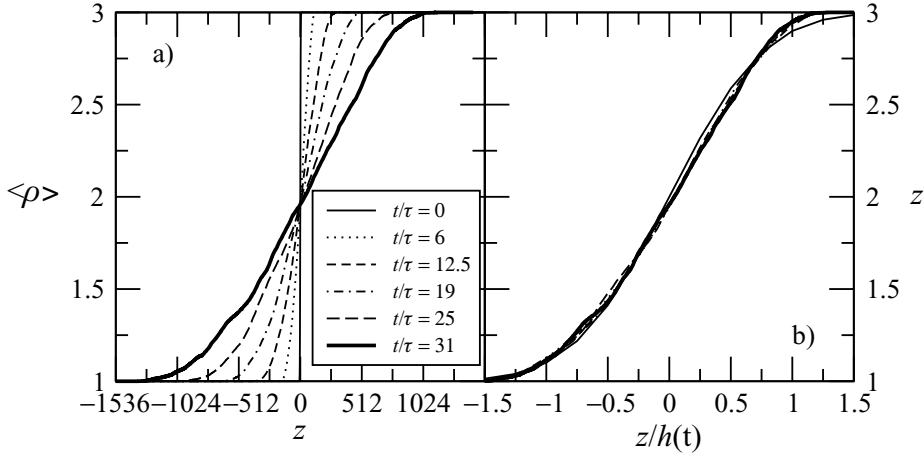


Figure 6. Mean density at different times as a function of (a) vertical plane number and (b) scaled vertical position.

3.4.2. Density variance and mean pressure gradient

The density intensity peaks on the light fluid side and its profile does not change much in time (Figure 8(a)). The Boussinesq limit corresponds to $\rho_{\text{rms}}/\bar{\rho} \rightarrow 0$ and a value of 0.05 is usually taken to define this limit. According to this, variable density effects, though modest at 0.25, are important in most of the layer. Below, it is shown that, even at low density intensities, there are non-negligible non-Boussinesq effects at the edges of the layer.

The density specific volume correlation, b , mediates the mass flux production mechanism, unlike the Boussinesq case where this role is played by the density variance [3]. Since, as is shown below, the mass flux is essential in setting the energy conversion rate, differences between b and the normalized density variance lead to structural flow changes between VD and Boussinesq cases and are indicative of non-Boussinesq effects. Figure 9 shows the b profiles across the layer at several times. Similar to density intensity, b peaks

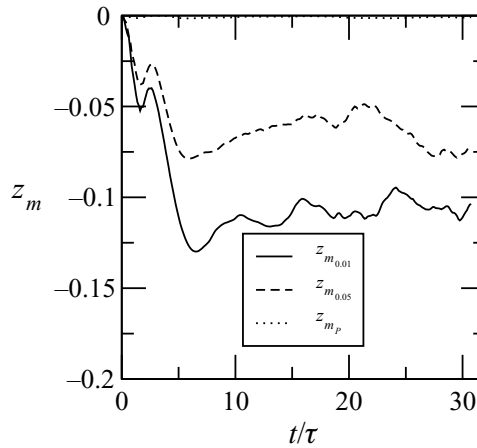


Figure 7. Vertical variation of the half-layer position, z_m , scaled by h .

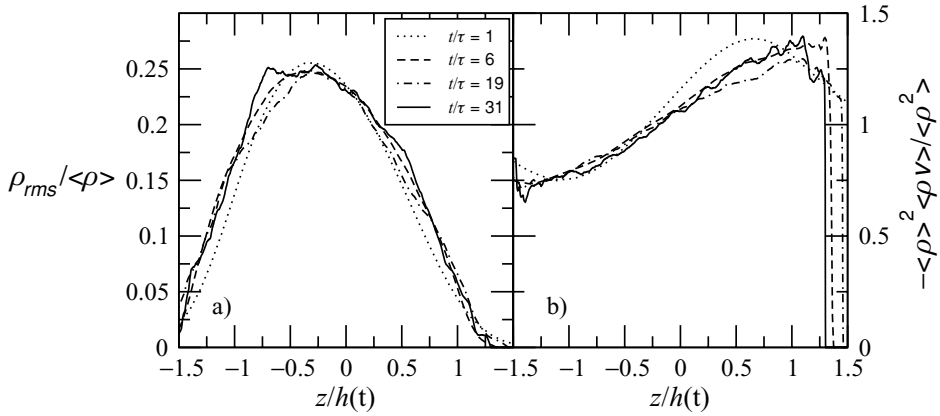


Figure 8. (a) Density intensity $i_\rho = \rho_{rms}/\bar{\rho}$ and (b) ratio of b to the square of density intensity across the layer at different times.

on the light fluid side. After the early times, b collapses quite well across the layer and becomes spatially self-similar.

Taking moments of the Taylor series of $v = v(\rho)$ about $v^* = V$, it is straightforward to show [2]

$$\langle\rho v\rangle = -\frac{\langle\rho^2\rangle}{\bar{\rho}^2} \left[1 - i_\rho \frac{\langle\rho^3\rangle}{\langle\rho^2\rangle^{3/2}} + i_\rho^2 \frac{\langle\rho^4\rangle}{\langle\rho^2\rangle^2} - i_\rho^3 \frac{\langle\rho^5\rangle}{\langle\rho^2\rangle^{5/2}} + \dots \right], \quad i_\rho = \frac{\langle\rho^2\rangle^{1/2}}{\bar{\rho}}. \quad (36)$$

The successive normalized moments are called skewness, kurtosis, hyperskewness, etc. As $i_\rho \rightarrow 0$, the formula reduces to the Boussinesq relation:

$$\langle\rho v\rangle = -\frac{\langle\rho^2\rangle}{\bar{\rho}^2}. \quad (37)$$

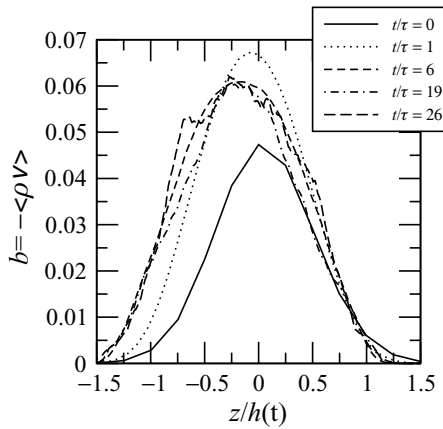


Figure 9. b variation across the layer.

The density PDF is skewed on either side of the centerline with negative skewness on the heavy fluid side and positive on the light fluid side, as few less mixed fluid regions approach the opposed side of the layer. Thus, away from the centerline all odd terms in the expansion (36) have the same sign. Therefore, even though i_ρ is small toward the edges, the departure from the Boussinesq formula (37) is largest at the edges of the layer, consistent with Figure 8(b).

$\langle \rho v \rangle$ and $\frac{\langle \rho^2 \rangle}{\bar{\rho}^2}$ mediate the production of the mass flux, which sets the energy conversion rate (see below and [3]) in the VD and Boussinesq cases, respectively. On the heavy fluid side, $\langle \rho v \rangle$ has larger magnitude than $\frac{\langle \rho^2 \rangle}{\bar{\rho}^2}$; on the light fluid side has smaller magnitude. Therefore, the Boussinesq equations lead to larger energy conversion rate in the light fluid side and smaller on the heavy fluid side, compared to the VD equations, when used for the same density differences. Since solving the Boussinesq equations is, in general, less expensive than solving the VD equations, one would like to use these equations for as large density differences as possible. The arguments above suggest that a good criterion for the validity of the results using the Boussinesq approximation is the emergence of asymmetries in the mixing layer.

The mean pressure gradient exhibits only modest non-Boussinesq effects (Figure 10(a)). However, the departure from the hydrostatic pressure head is partially responsible for the asymmetry of the turbulent kinetic energy. The other factor contributing to this asymmetry is the fixed point in the mean density profile. The largest departures, of about 10%, are obtained away from the centerline and the edges. After the early times ($t/\tau > 6$), $P_{,3}/(\bar{\rho} g_3)$ changes little in time. Figure 10(b) shows that the mean pressure gradient is close to the formula used in the homogeneous simulations of [2, 3].

3.5. Mean velocities and mass flux asymmetries

For immiscible incompressible fluids $\frac{\partial U_3}{\partial z} = 0$ and since $U_3 = 0$ outside the layer, it yields $U_3 = 0$ everywhere. For the miscible case the divergence of the velocity is not zero. In the present Rayleigh–Taylor configuration, $U_1 = U_2 = 0$ and $U_3 = -\frac{1}{ReSc} \langle \frac{\partial(\ln \rho^*)}{\partial z} \rangle$. Thus, the

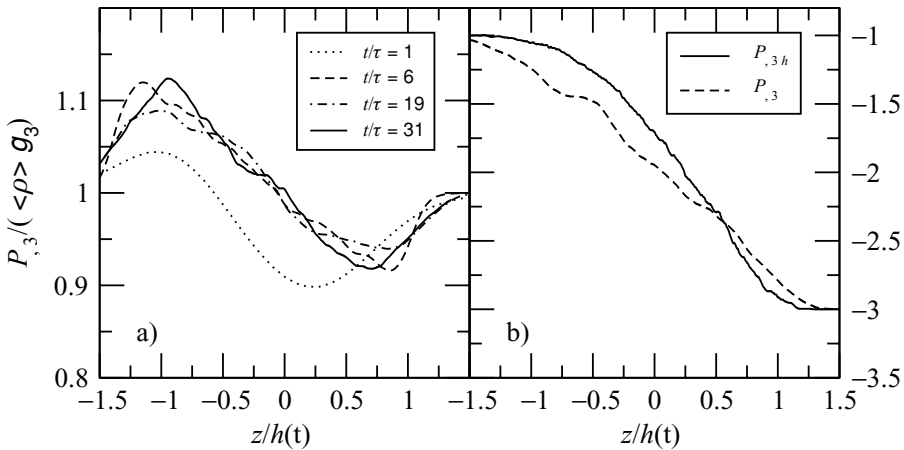


Figure 10. (a) Mean pressure gradient normalized by the pressure head and (b) mean pressure gradient compared to the formula used in the homogeneous simulations of [2, 3], $P_{,3h} = \frac{1}{V}(g_3 - \langle v p_{,i} \rangle + \langle u_i u_{j,j} \rangle + \langle v \tau_{ij,j} \rangle)$. For clarity, the results have been smoothed by applying a running average.

mean velocity is purely dilatational and arises solely due to the molecular mixing. In fact, U_3 can be related to the (interspecies) diffusion velocity, V_3 , by $U_3 = -\langle V_3(\rho_2 - \rho)/\rho_2 \rangle$. At very early times, when the density gradients are sharp, U_3 is important. However, after the initial instant, the Reynolds mean velocity is small so that $\tilde{U}_3 \approx a_3$.

A fixed point in the mean density profile, $\bar{\rho}_{,t} = 0$, is observed to occur at $z = 0$ (see above). From the mean continuity equation (14) this leads to $\frac{\partial}{\partial z}(\bar{\rho} \tilde{U}_3) = 0$ at $z = 0$ and, thus, $\bar{\rho} \tilde{U}_3$ is maximum in magnitude (note $\tilde{U}_3 < 0$) at $z = 0$. As the mean density increases with the height z , \tilde{U}_3 (and a_3) has its minimum value (maximum in magnitude) below the centerline (Figure 11(a)).

\tilde{U}_3 at the centerline and maximum \tilde{U}_3 both increase linearly in magnitude after $t/\tau \approx 6$ (Figure 11(b)), consistent with the time when $\alpha = \frac{\tilde{h}^2}{4Ag\eta}$ reaches a constant value [1].

Similar to the Favre mean kinetic energy, $\tilde{K} = 1/2 \tilde{U}_i \tilde{U}_i$, the Favre turbulent kinetic energy, \tilde{k} , profile peaks on the light fluid side (Figure 12(a)), which is shown below to also be related to the mean density profile features. Both the centerline and peak values of \tilde{k} increase quadratically in time after $t/\tau \approx 6$, consistent with the self-similarity of the flow (Figure 12(b)).

3.6. Anisotropy

Since buoyancy production is inherently anisotropic, it is expected that the normal stresses be anisotropic. A measure of the large scale anisotropy, which appears in the moment equations, is the Favre Reynolds stress anisotropy tensor:

$$b_{ij} = \frac{R_{ij}}{R_{kk}} - \frac{1}{3} \delta_{ij} \quad (38)$$

which is bounded by $-\frac{1}{3} \leq b_{ij} \leq \frac{2}{3}$. The lower bound for a diagonal component corresponds to no energy in that component and the upper bound, $\frac{2}{3}$, to 100% of the energy in that component. Similar to the Boussinesq case [11] and the homogeneous configuration [3],

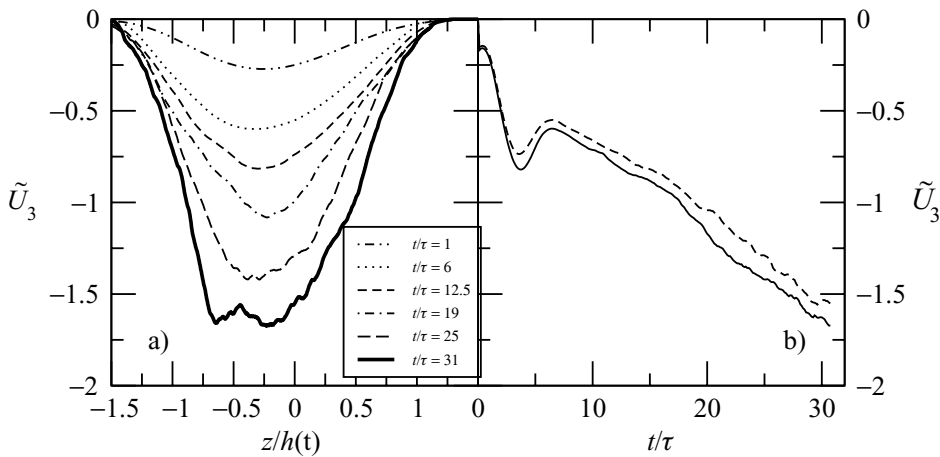


Figure 11. (a) Vertical variation of the Favre mean velocity \tilde{U}_3 at $t/\tau = 1, 6, 12.5, 19, 25$, and 31 . (b) Time variation of peak \tilde{U}_3 (continuous line) and \tilde{U}_3 at the centerline (dashed line).

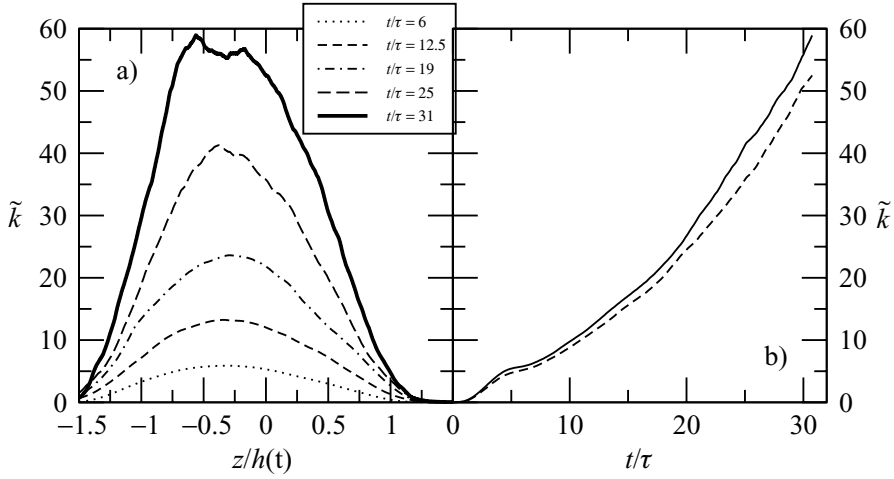


Figure 12. (a) Vertical profiles of the Favre turbulent kinetic energy at $t/\tau = 1, 6, 12.5, 19, 25$, and 31 . (b) Time evolution of peak \tilde{k} (continuous line) and \tilde{k} at the centerline.

the normal stresses are non-isotropic at all times (Figure 13). Note that for the present configuration, as well as HRT, b_{ij} defined based on the Favre Reynolds stresses is close to that defined based on the Reynolds stresses. b_{33} seems to become almost constant across the layer, with an asymptotic value $b_{33} \approx 0.3$ corresponding to $\approx 65\%$ energy in the vertical component. Values of $b_{33} \approx 0.3$ were also reported for the Boussinesq case at long times at the centerline by [11].

3.6.1. Scale dependence of the normal stresses anisotropy

It is generally believed that in high-Reynolds number flows the small scales become isotropic and decoupled from the large scales as, in general, production mechanisms tend to be confined to large scales. However, [2] showed that buoyancy production, even though it

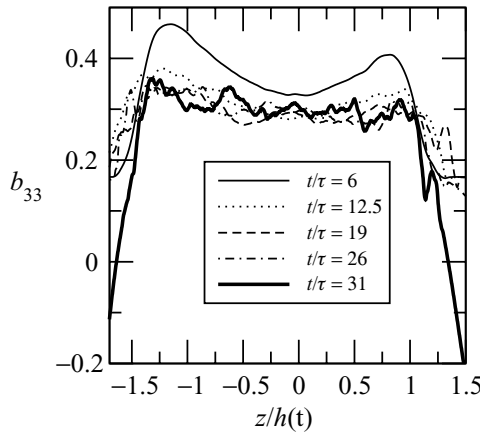


Figure 13. Vertical variation of b_{33} at different times.

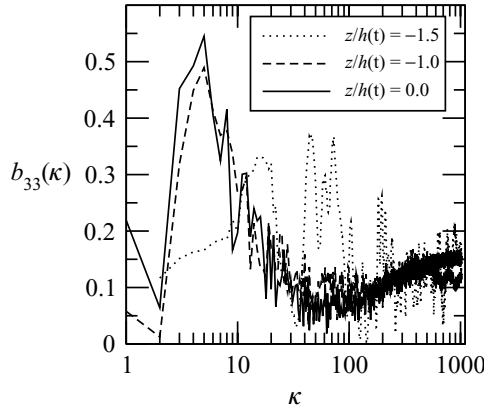


Figure 14. Wave number dependence of $b_{33}(\kappa)$ at different z locations.

becomes much smaller than the nonlinear transfer at large wave numbers, has a significant effect on the smallest scales of the flow during the kinetic energy growth stages in HRT. This is because in the viscous range there is a cancellation between nonlinear transfer and viscous dissipation so that buoyancy production leads to a persistent anisotropy of the normal stresses at these scales. This is substantiated by the fact that the dissipation itself tends to be more isotropic. As the small scales kinetic energy grows, the dissipation first increases in response to the rise in the nonlinear transfer and there is a lag between the increase in the buoyancy production and the response in the dissipation. Thus, Livescu and Ristorcelli [2] suggested that for buoyancy-driven flows, the viscous scales are not universal. However, in some intermediate range, far from the large scales dominated by buoyancy production and small scales where viscous dissipation starts to play a role, the normal stresses become close to isotropic, suggesting that an inertial range may develop.

The results regarding anisotropy found in HRT [2, 3] also hold for the RT configuration: the normal stresses tend to become isotropic only in some intermediate range (Figure 14). At the largest and smallest scales, the normal stresses remain anisotropic. Unexpectedly, at the smallest scales, $b_{33}(\kappa) \approx 0.15$ (which is close to the HRT value at similar A and Sc), corresponding to $\approx 50\%$ energy in the vertical component. Similar to HRT, however, the dissipation itself becomes more isotropic at long times [1], supporting the suggestion that, due to the cancellation between nonlinear transfer and viscous dissipation, the buoyancy production remains important at small scales.

3.7. Energy conversion

Kinetic energy is produced in the flow because there is net available potential energy. The available potential energy inside a control volume is

$$E_p^*(t) = -\frac{g_i}{\mathcal{V}} \int_{\mathcal{V}} (\rho^* - \rho_0) x_i dV, \quad (39)$$

where ρ_0 is the density in the final (equilibrium) state. The rate of change of the potential energy is the sum of the time rate of change of the potential energy inside the control volume

and the flux of potential energy through the boundaries. To obtain the vertical variation, the control volume is defined having an infinitesimal extent δz in the vertical direction:

$$\begin{aligned}
 \frac{\partial}{\partial t} \mathcal{E}(z, t) &= \frac{\partial}{\partial t} E_p^* + \mathcal{F}_{E_p^*} \\
 &= -\frac{\partial}{\partial t} \left(\frac{g_i}{\mathcal{S}\delta z} \int_{\mathcal{V}} (\rho^* - \rho_0) x_i d\mathcal{V} \right) - \frac{g_i}{\mathcal{S}\delta z} \int_{\mathcal{S}} (u_j^* \rho^* - u_{j\text{equil}}^* \rho_0) x_i d\mathcal{S}_j \\
 &= \frac{g_i}{\mathcal{S}\delta z} \int_{\mathcal{V}} (\rho^* u_j^*)_{,j} x_i d\mathcal{V} - \frac{g_i}{\mathcal{S}\delta z} \int_{\mathcal{S}} (u_j^* \rho^* - u_{j\text{equil}}^* \rho_0) x_i d\mathcal{S}_j \\
 &= -\frac{g_i}{\mathcal{S}\delta z} \int_{\mathcal{V}} \rho^* u_i^* d\mathcal{V} + \frac{g_i \rho_0}{\mathcal{S}\delta z} \int_{\mathcal{S}} u_{j\text{equil}}^* x_i d\mathcal{S}_j \\
 &= -\frac{g_3}{\delta z} \langle \rho^* u_3^* \rangle \delta z + g_3 \rho_0 U_{3\text{equil}} \\
 &= -g_3 \bar{\rho} \tilde{U}_3 \approx -g_3 \bar{\rho} a_3.
 \end{aligned} \tag{40}$$

$U_{3\text{equil}}$ accounts for an eventual solid body motion in the equilibrium state, when $\rho^* = \bar{\rho}$. For the present configuration, with wall-bounded domain, it is zero. The expression above is the same as in the homogeneous configuration [3]. At each z level, the rate of conversion of potential into kinetic energy is proportional to the normalized mass flux. In addition, since $-\bar{\rho} \tilde{U}_3$ has the largest value at $z = 0$, the energy conversion rate is maximum at the centerline.

4. Energy budgets of the second moment equations

The energy budgets for the Favre turbulent kinetic energy, \tilde{k} , normalized mass flux, a_i , density specific volume correlation, b , and mass fraction, Y_m , transport equations are now examined. These equations are relevant to a second-order moment closure of the flow, so the information presented also represents an archival database for model testing. Issues related to the ability of gradient transport hypothesis to describe the turbulence transport are then investigated. As the data become noisy at late times, a running average was used in all late time plots for clarity.

4.1. Kinetic energy equation budget

The transport equations for the Favre mean and turbulent kinetic energies for the current configuration can be easily derived from Equations (17) and (31):

$$\begin{aligned}
 \frac{\partial}{\partial t} (\bar{\rho} \tilde{K}) &= -(\bar{\rho} \tilde{U}_3 \tilde{K})_{,3} - (\tilde{U}_3 R_{33})_{,3} + \bar{\rho} \tilde{U}_3 g_3 - \tilde{U}_3 P_{,3} + R_{33} \tilde{U}_{,3} + \tilde{U}_3 \bar{\tau}_{33,3}, \tag{41} \\
 \frac{\partial}{\partial t} (\bar{\rho} \tilde{k}) &= \underbrace{-(\bar{\rho} \tilde{U}_3 \tilde{k})_{,3}}_I + \underbrace{+a_3 P_{,3}}_{II} - \underbrace{R_{33} \tilde{U}_{,3}}_{III} - \underbrace{a_3 \bar{\tau}_{33,3}}_{IV} - \underbrace{\frac{1}{2} R_{ii3,3}}_V \\
 &\quad - \underbrace{\langle u_3 p \rangle_{,3}}_{VI} + \underbrace{\langle u_i \tau_{i3} \rangle_{,3}}_{VII} + \underbrace{\langle p d \rangle_{,3}}_{VIII} - \underbrace{\langle \tau_{ij} u_{i,j} \rangle}_{IX}.
 \end{aligned} \tag{42}$$

Figure 15 shows the terms in the Favre turbulent kinetic energy equation at different times. The mean Favre kinetic energy production term, $\bar{\rho} \tilde{U}_3 g_3$, is exactly the negative of the potential energy rate of change (40). Thus, potential energy is directly converted into Favre mean kinetic energy. Energy is then transferred to Favre turbulent kinetic energy by the mass flux mean pressure gradient product ($a_3 P_{,3}$) and also to and from mean kinetic energy by $-R_{33} \tilde{U}_{3,3}$. As the mean shear is zero in this flow, the mean velocity gradient term is not a net production mechanism for turbulent kinetic energy, so that $-R_{33} \tilde{U}_{3,3}$ can have either sign.

The production term $a_3 P_{,3}$, is the largest term in Equation (42), underlying the fundamental role of the mass flux in the energy conversion mechanism. It is shown above that the fixed point in the mean density profile implies that $\bar{\rho} \tilde{U}_3$ (and $\bar{\rho} a_3$) peaks at the centerline. In addition, the mean pressure gradient is larger than the hydrostatic head, $\bar{\rho} g$, in the light

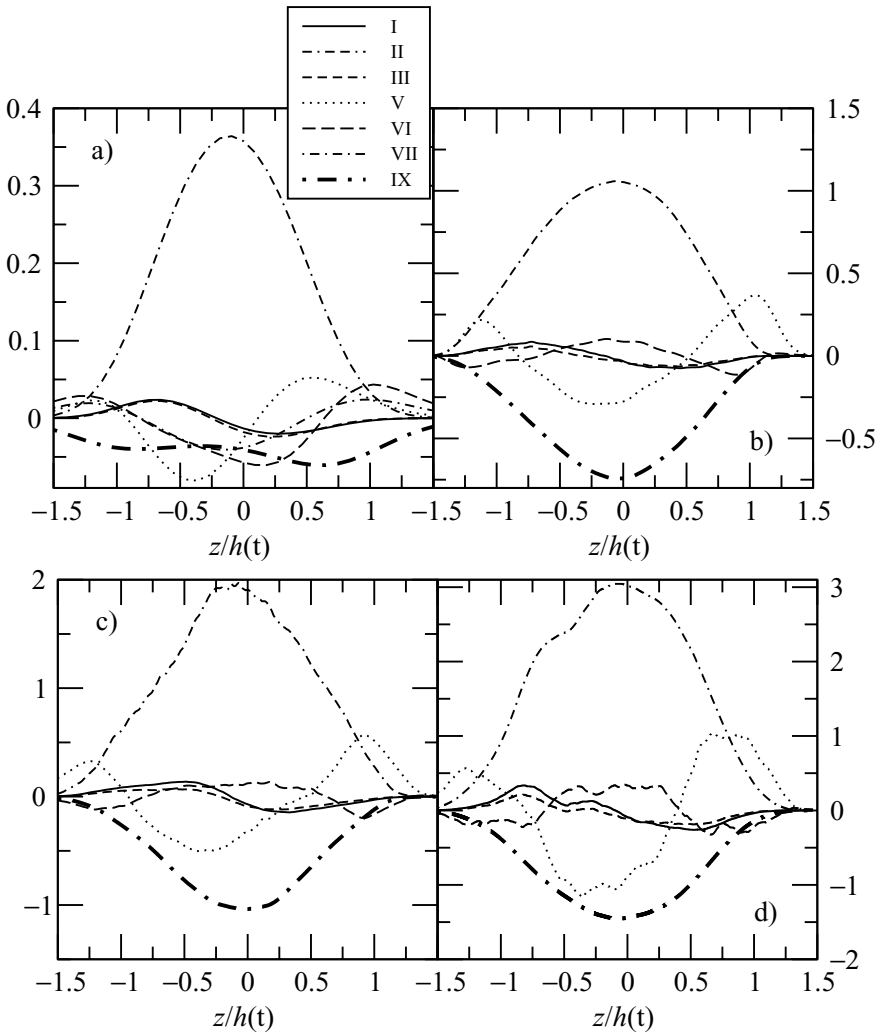


Figure 15. Terms in the Favre turbulent kinetic energy equation: (a) $t/\tau = 1$, (b) $t/\tau = 6$, (c) $t/\tau = 19$, and (d) $t/\tau = 31$.

fluid side and smaller in the heavy fluid side (although by small amounts at the moderate Atwood number of this flow). Therefore, as shown in Figure 15, term II, $a_3 P_{,3}$, has the largest magnitude slightly off the centerline, on the light fluid side. The mean velocity gradient (term III) transfers energy from the mean flow to turbulence on the light fluid side and vice versa on the heavy fluid side. Thus, the $\bar{\rho} \tilde{k}$ production is largest on the light fluid side. This leads to an asymmetry in $\bar{\rho} \tilde{k}$ and even larger asymmetry in Favre turbulent kinetic energy profiles (Figure 12(a)).

The transport terms I, V, VI, and VII redistribute the energy inside the layer. Term I transports energy from heavy to light fluid sides, contributing to the kinetic energy asymmetry, V from interior of the layer to the edges (main mechanism for the spreading of the turbulent kinetic energy), and VI back from the edges to the interior (opposes the spread of the layer). As more energy is produced in the light fluid side, term V also has larger magnitudes below the centerline (negative in the largest production region and positive toward the edge). This is consistent with the asymmetry between the bubble and spike fronts discussed earlier. The last transport term, VII, becomes small after the very early times.

Interestingly, the viscous dissipation (term IX) remains symmetrical with respect to the centerline throughout the evolution of the flow. The non-Boussinesq effects primarily affecting the asymmetry of the flow are large scale and manifest in the asymmetry of the mean pressure gradient and Favre mean velocity.

The rest of the terms in Equation (42), terms IV and VIII (pressure dilatation), become small after the initial times.

In summary, the leading order energy balances in the high Re (late time) regime, with their magnitude relative to the time derivative, are as follows:

RT layer interior

$$\frac{\partial}{\partial t} \bar{\rho} \tilde{k} = \underbrace{+a_3 P_{,3}}_{II \ (\approx 3)} - \underbrace{\langle \tau_{ij} u_{i,j} \rangle}_{IX \ (\approx -1.5)} - \underbrace{\frac{1}{2} R_{ii3,3}}_{V \ (\approx -1)} - \underbrace{\langle u_3 p \rangle_{,3}}_{VI \ (\approx 0.5)} + \dots \quad (43)$$

RT layer edges

$$\frac{\partial}{\partial t} \bar{\rho} \tilde{k} = \underbrace{-\frac{1}{2} R_{ii3,3}}_{V \ (\approx 1)} + \dots \quad (44)$$

The important terms which need closure in Equation (42) are the dissipation (term IX) and the transport term V. As a transport equation for dissipation is overly cumbersome, most single point closures model it either by assuming some similarity (through a timescale) with the kinetic energy, or considering a phenomenological transport equation. Below, it is shown that the dissipation lags behind the kinetic energy, for the duration of the simulation, and does not attain a similar self-similar state with the kinetic energy. Thus, a dissipation transport equation is required to capture the dissipation evolution in this flow. The turbulence transport terms are usually closed using a gradient transport hypothesis and such models are examined in Section 4.4.

4.2. Mass flux equation budget

The transport equation for the mass flux in the vertical direction, for the present configuration, is

$$\begin{aligned}
 \frac{\partial}{\partial t} (\bar{\rho} a_3) = & \underbrace{-(\bar{\rho} \tilde{U}_3 a_3)_{,3}}_I + \underbrace{b(P_{,3} - \bar{\tau}_{33,3})}_{II} + \underbrace{\bar{\rho} (\langle vp_{,3} \rangle - \langle v \tau_{3j,j} \rangle)}_{III} \\
 & \underbrace{-\bar{\rho} a_3 (\tilde{U}_3 - a_3)_{,3}}_{IV} + \underbrace{\frac{\bar{\rho}_{,3}}{\bar{\rho}} (\langle \rho u_3^2 \rangle - R_{33})}_{V} + \underbrace{\bar{\rho} (a_3^2)_{,3}}_{VI} \\
 & \underbrace{-(\langle \rho u_3^2 \rangle_{,3})}_{VII} + \underbrace{\bar{\rho} \langle u_3 d \rangle}_{VIII}.
 \end{aligned} \tag{45}$$

Figure 16 shows the terms in the mass flux equation at different times. Barring the statistical variability, the production, terms II and V, and destruction, term III, are symmetrical with respect to the centerline. This is consistent with the fixed point found above in the mean density profile, which required that $\bar{\rho} a_3$ peaked at the centerline and the normalized mass flux itself on the light fluid side. The two production terms have relatively close magnitude, with term II the largest between the two. This term depends directly on the fluid configuration (or the mix state) through b .

The transport terms I and VI have opposite sign and close magnitude. Term I transports the mass flux from the heavy to light fluid sides while term VI increases $\bar{\rho} a_3$ on the heavy fluid side. The velocity dilatation part of term VII becomes small after very early times, while the transport part moves mass flux from the interior toward the edges and is responsible for the spreading of the mass flux.

After the very early times, the destruction term III becomes the largest term in the interior of the layer. This term represents a direct manifestation of non-Boussinesq effects, as the fluctuating pressure gradient is directly proportional to departures from the hydrostatic pressure head.

In summary, the leading order mass flux balances in the high Re (late time) regime, with their magnitude relative to the time derivative, are as follows:

RT layer interior

$$\begin{aligned}
 \frac{\partial}{\partial t} (\bar{\rho} a_3) = & \underbrace{+\bar{\rho} \langle vp_{,3} \rangle}_{III \ (\approx 19)} + \underbrace{+bP_{,3}}_{II \ (\approx -15)} - \underbrace{\frac{\bar{\rho}_{,3}}{\bar{\rho}} R_{33}}_{V \ (\approx -11)} \\
 & \underbrace{-\langle \rho u_3^2 \rangle_{,3}}_{VII \ (\approx 6)} + \dots
 \end{aligned} \tag{46}$$

RT layer edges

$$\frac{\partial}{\partial t} (\bar{\rho} a_3) = \underbrace{-\langle \rho u_3^2 \rangle_{,3}}_{VII \ (\approx 1)} + \dots \tag{47}$$

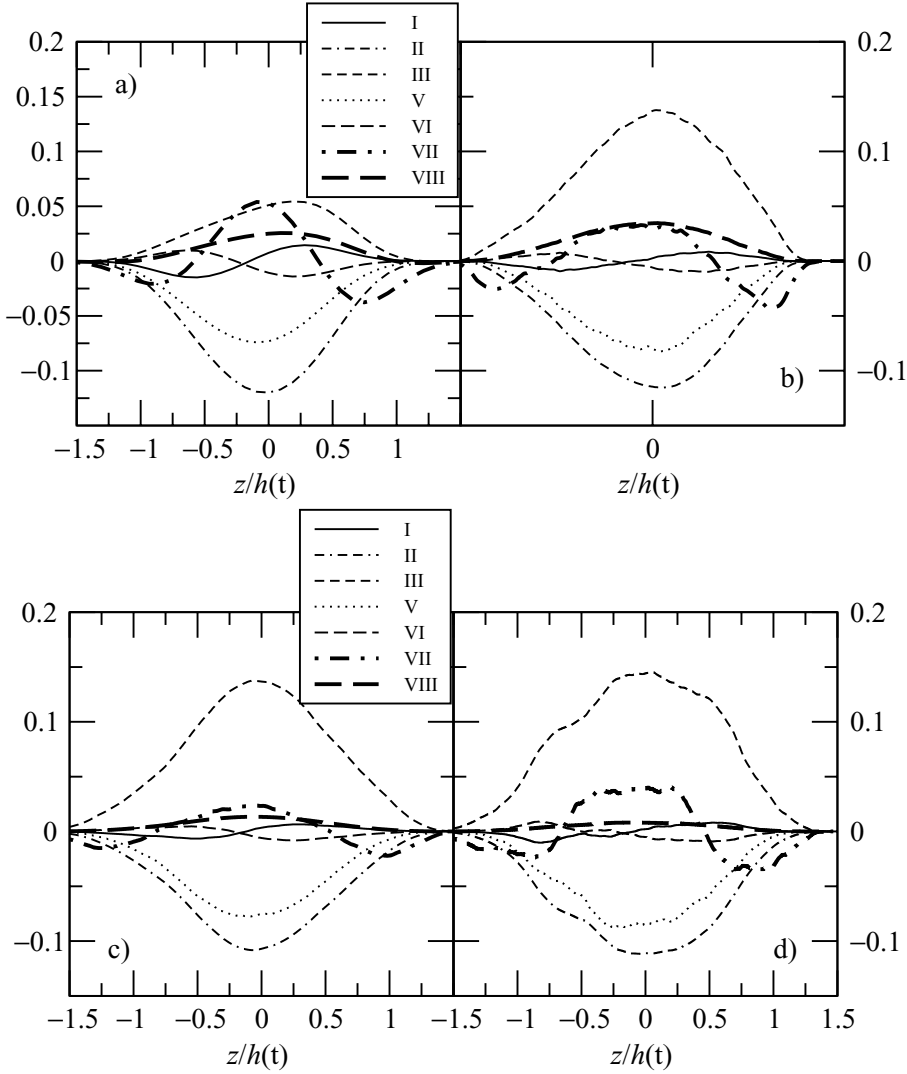


Figure 16. Terms in the normalized mass flux, a_3 , transport equation (a) $t/\tau = 1$, (b) $t/\tau = 6$, (c) $t/\tau = 19$, and (d) $t/\tau = 31$.

4.2.1. Modeling issues

At the centerline, the four leading order terms are much larger than the time derivative. Thus, a quasi-equilibrium assumption in which the left-hand side of Equation (45) is set to zero appears appealing. However, it was shown before that the mass flux is not constant and increases linearly in time, consistent with the Boussinesq self-similar analysis of [11]. Therefore, the quasi-equilibrium assumption, $\frac{\partial}{\partial t}(\bar{\rho} a_3) \approx 0$, is not valid. Modeling equation (45) imposes unique challenges, as the mass flux time variation is given by a delicate balance of large terms.

After the initial times, as mixed fluid occupies large areas inside the layer, the specific volume pressure gradient (part of term III), which acts as a destruction term for the mass

flux, dominates the balance in Equation (45). Thus, an accurate model for $\langle vp_{,3} \rangle$ is essential for predicting the mass flux; this is the subject of current research.

The production term, $bP_{,3}$, is crucial to the prediction of the sign change of the mass flux when the mean pressure changes sign in response to a change in the body force. In flows with significant amounts of non-mixed fluids, this term is largest in Equation (45) and sets the mass flux rate of change. If the fluids are mostly mixed, then b is small and $bP_{,3}$ does not produce the differential accelerations that generate the mass flux. Closing $bP_{,3}$ requires a model or transport equation for b ; this is discussed next.

The largest contribution to term V comes from R_{33} ; its usual modeling in terms of the kinetic energy requires knowledge of the large scale anisotropy, discussed above. The triple correlation $\langle \rho u_3^2 \rangle$ represents the largest part of term VII and appears in divergence form. Gradient transport hypotheses for $\langle \rho u_3^2 \rangle$ are explored in Section 4.4.

4.3. Density specific volume correlation equation budget

The transport equation for b , for the present configuration, is

$$\frac{\partial}{\partial t} b = \underbrace{-\tilde{U}_3 b_{,3}}_I + \underbrace{+2a_3 b_{,3}}_{II} - \underbrace{2a_3(1+b)\frac{\bar{\rho}_{,3}}{\bar{\rho}}}_{III} + \underbrace{\bar{\rho} \left(\frac{\langle u_3 \rho v \rangle}{\bar{\rho}} \right)_{,3}}_{IV} - \underbrace{+2\bar{\rho} \langle vd \rangle}_V. \quad (48)$$

Figure 17 shows the terms in the b equation at different times. The production term III peaks on the light fluid side, a direct consequence of the fixed point at $z = 0$ in the mean density profile. Thus, $a_3 \bar{\rho}$ peaks at the centerline and therefore $a_3 \bar{\rho}_{,3}$ has the largest magnitude below the centerline. The asymmetry of the production of b leads to the asymmetry of b shown earlier.

Terms I and II redistribute b across the layer (term I from the heavy fluid side to the light fluid side and term II vice versa) and become small after the initial instant. Term IV transports b toward the edge regions, representing the main mechanism for the spreading of the b profile. Term V represents the destruction of b . Unlike the destruction terms in \bar{k} and a_3 equations, term V is also asymmetric with respect to the centerline.

In summary, the leading order b balances in the high Re (late time) regime, with their relative magnitude compared to the largest term on the right-hand side of the equation, are

RT layer interior

$$0 = \underbrace{-2a_3(1+b)\frac{\bar{\rho}_{,3}}{\bar{\rho}}}_{III \ (\approx 1)} + \underbrace{+2\bar{\rho} \langle vd \rangle}_V \ (\approx -0.75) + \underbrace{\bar{\rho} \left(\frac{\langle u_3 \rho v \rangle}{\bar{\rho}} \right)_{,3}}_{IV \ (\approx -0.25)} + \dots. \quad (49)$$

RT layer edges

$$\frac{\partial}{\partial t} b = \underbrace{\bar{\rho} \left(\frac{\langle u_3 \rho v \rangle}{\bar{\rho}} \right)_{,3}}_{IV \ (\approx 1)} + \dots. \quad (50)$$

The unclosed terms in the b equation are $\langle vd \rangle$ and the triple correlation, $\langle u_3 \rho v \rangle$. A modeling strategy for $\langle vd \rangle$ is not discussed here and is the subject of future work. Gradient transport hypotheses for $\langle u_3 \rho v \rangle$ are explored in Section 4.4.

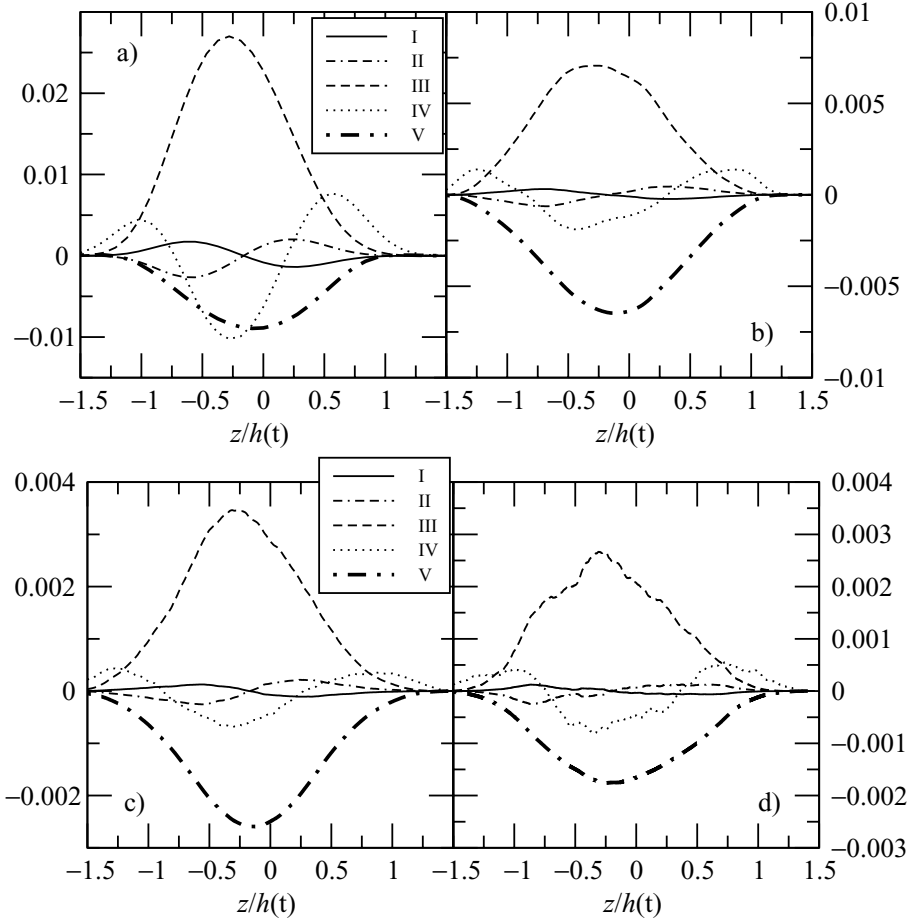


Figure 17. Terms in the b transport equation (a) $t/\tau = 1$, (b) $t/\tau = 6$, (c) $t/\tau = 19$, and (d) $t/\tau = 31$.

4.4. Investigating the gradient transport hypothesis

In this section, the popular gradient transport hypothesis for the turbulent transport terms in the moment equations is investigated. Usually, the eddy viscosity is modeled using the time and lengthscales defined based on the kinetic energy and dissipation, $\tau_t = \tilde{k}/\varepsilon$ and $l = \tilde{k}^{3/2}/\varepsilon$, since these quantities are readily available in one-dimensional models, resulting in $\nu'_t = (C_\mu/\sigma_t)\tilde{k}^2/\varepsilon$.

The variation of \tilde{k}^2/ε across the layer was discussed above, as this quantity is proportional to Re_t . It was shown that, throughout the simulation and long after the onset of self-similar growth, Re_t is not proportional to $h^{2/3}$, as required by asymptotic self-similarity. It was also shown that l does not represent the true integral scale as the Kolmogorov's zeroth law is not satisfied. Similar to l , the eddy turnover time τ_t is not constant across the layer (Figure 18(a)). There is a minimum value which occurs around the centerline and τ_t becomes very large toward the edges, where the dissipation decreases to zero faster than the kinetic energy.

Below it is shown that the transport terms are better described using $\nu''_t = (C_\mu/\sigma_t)h\tilde{k}^{1/2}$ instead of ν'_t as the eddy viscosity in the gradient transport hypothesis. This is a consequence

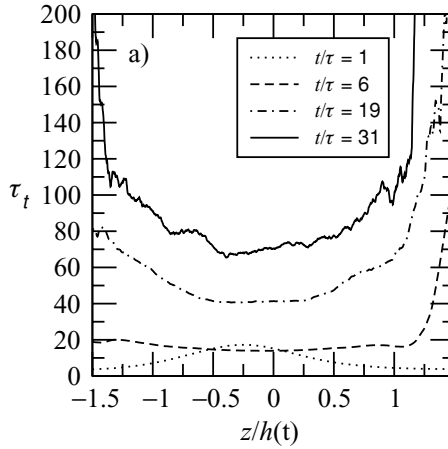


Figure 18. Vertical profiles of $\tau_t = \tilde{k}/\varepsilon$ at $t/\tau = 1, 6, 19$, and 31 .

of the transient spectral dynamics, occurring even after the flow becomes self-similar: the dissipation still lags the large scale energy production.

4.4.1. Mass flux

The gradient transport hypothesis for the mass flux, which appears in divergence form in the mean continuity equation, is

$$\bar{\rho} a_3 = \langle \rho u_3 \rangle = -v_t \bar{\rho}_{,3}, \quad (51)$$

where v_t is usually taken to be a constant or $v_t = v'_t = C_\mu/\sigma_t \tilde{k}^2/\varepsilon$. Figure 19 clearly shows that a constant v_t is not justified. More importantly, the match using $v_t = v'_t$ is very poor in time, although at later times the spatial variation is relatively well captured away from the edges. The main reason for this mismatch is the lag between the evolution of the dissipation and the increase in large scale energy. However, $\langle \rho u_3 \rangle$ seems to follow surprisingly well $-(C_\mu/\sigma_t h) \sqrt{\tilde{k}} \bar{\rho}_{,3}$ with $C_\mu/\sigma_t \approx 0.39$ changing little in time. The C_μ/σ_t value calculated using H_b instead of h is ≈ 0.33 , which is slightly higher than the 0.288 value reported by [17] and much larger than the standard value for shear flows, 0.09 [15].

4.4.2. Kinetic energy equation

Term V in Equation (42) is important both at the center and edges of the layer and is unclosed. The term can be rewritten as $R_{ii3,3} = (\bar{\rho} R_{ii3}/\bar{\rho})_{,3}$. The gradient transport hypothesis, in this case, is

$$R_{ii3}/\bar{\rho} = -v_t \tilde{k}_{,3}. \quad (52)$$

Neither option for v_t (v'_t or v''_t) works as well as for the mass flux, however $-(C_\mu/\sigma_t) h \sqrt{\tilde{k}} \tilde{k}_{,3}$ gives a fit for $R_{ii3}/\bar{\rho}$ which is less dependent on time (Figure 20).

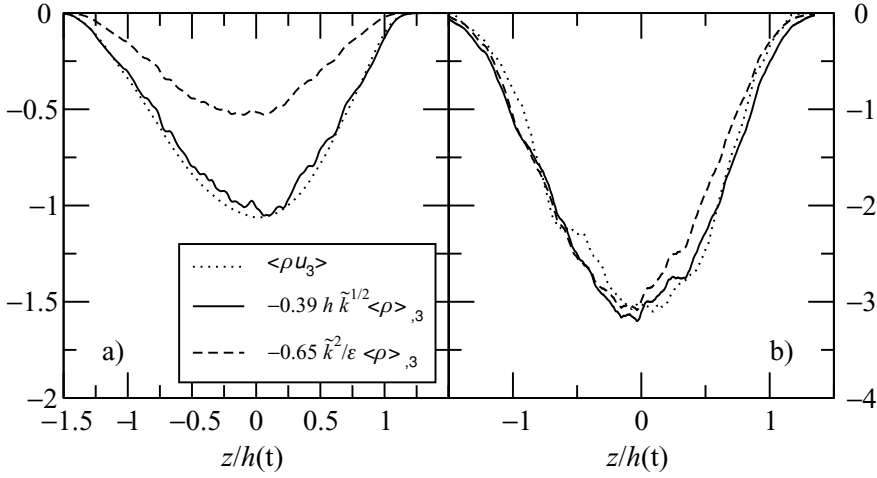


Figure 19. Comparison of $\langle \rho u_3 \rangle$ across the layer with a gradient transport hypothesis, $-0.39 h \sqrt{\tilde{k}} \bar{\rho}_{,3}$ and $-0.65 \tilde{k}^2 / \varepsilon \bar{\rho}_{,3}$ at a) $t/\tau = 6$, b) $t/\tau = 31$. The coefficients were chosen to provide a good fit in the interior of the layer at $t/\tau = 31$.

4.4.3. Mass flux equation

The term $\langle \rho u_3^2 \rangle_{,3}$ is an important term in Equation (45) and is unclosed. The term can be rewritten as $\langle \rho u_3^2 \rangle_{,3} = (\bar{\rho} \langle \rho u_3^2 \rangle / \bar{\rho})_{,3}$. The gradient transport hypothesis becomes in this case:

$$\langle \rho u_3^2 \rangle / \bar{\rho} = -v_t a_{3,3}. \quad (53)$$

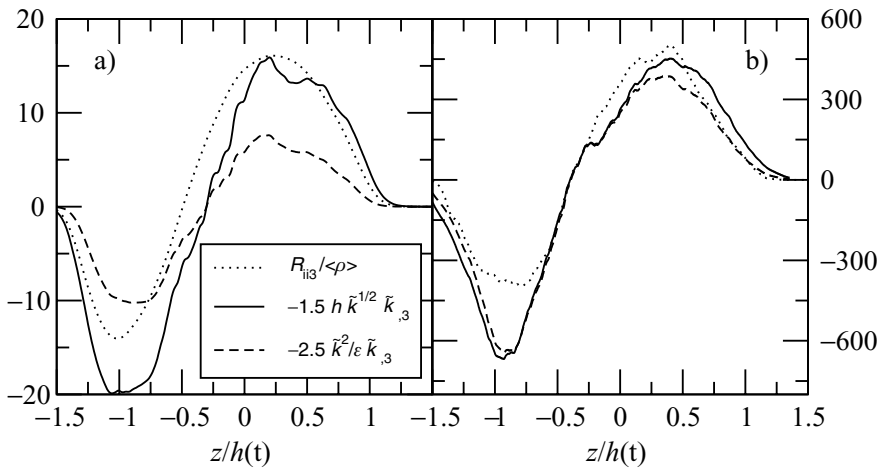


Figure 20. Comparison of $R_{ii3}/\bar{\rho}$ across the layer with a gradient transport hypothesis, $-1.5 h \sqrt{\tilde{k}} \tilde{k}_{,3}$ and $-2.5 \tilde{k}^2 / \varepsilon \tilde{k}_{,3}$ at a) $t/\tau = 6$ and b) $t/\tau = 31$. The coefficients were chosen to provide a good fit in the interior of the layer at $t/\tau = 31$.

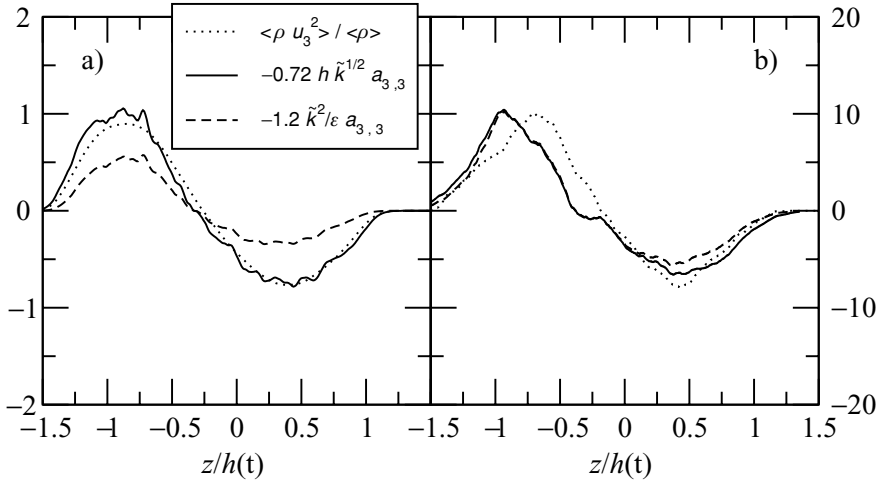


Figure 21. Comparison of $\langle \rho u_3^2 \rangle / \bar{\rho}$ across the layer with a gradient transport hypothesis, $-0.72 h \sqrt{\tilde{k}} a_{3,3}$ and $-1.2 \frac{\tilde{k}^2}{\varepsilon} a_{3,3}$ at (a) $t/\tau = 6$ and (b) $t/\tau = 31$. The coefficients were chosen to provide a good fit in the interior of the layer at $t/\tau = 31$.

Similar to the mass flux, the turbulent eddy diffusivity given by $(C_\mu/\sigma_t)h\sqrt{\tilde{k}}$ seems to work better than $(C_\mu/\sigma_t)\tilde{k}^2/\varepsilon$, as the former option provides a C_μ/σ_t which changes little in time (Figure 21).

4.4.4. b equation

Term IV, which contains a triple correlation and needs closure, is an important term in the b equation. The gradient transport hypothesis for this term is

$$\langle \rho v u_3 \rangle = -\nu_t b_{,3}. \quad (54)$$

The data are noisy at long times, but it seems that $\langle \rho v u_3 \rangle$ scales better across the layer with $-h\sqrt{\tilde{k}}b_{,3}$ than with $-\frac{\tilde{k}^2}{\varepsilon}b_{,3}$ (Figure 22). As with the other transport terms examined, the fit with $-h\sqrt{\tilde{k}}b_{,3}$ also changes little in time.

4.4.5. Mass fraction transport equation

For variable density (incompressible) two fluid mixing, the density and mass fractions are not independent. Using (1), the mass fraction flux can be written for the present configuration as

$$\Upsilon_{13} = -\Upsilon_{23} = -\frac{\rho_2 \rho_1}{\rho_2 - \rho_1} a_3. \quad (55)$$

Thus, the mass fraction flux is directly proportional to the mass flux. If a model is provided for the mass flux, the same model should be used for the mass fraction flux; if a transport equation is considered for a_3 , then the mass fraction flux is no longer unclosed.

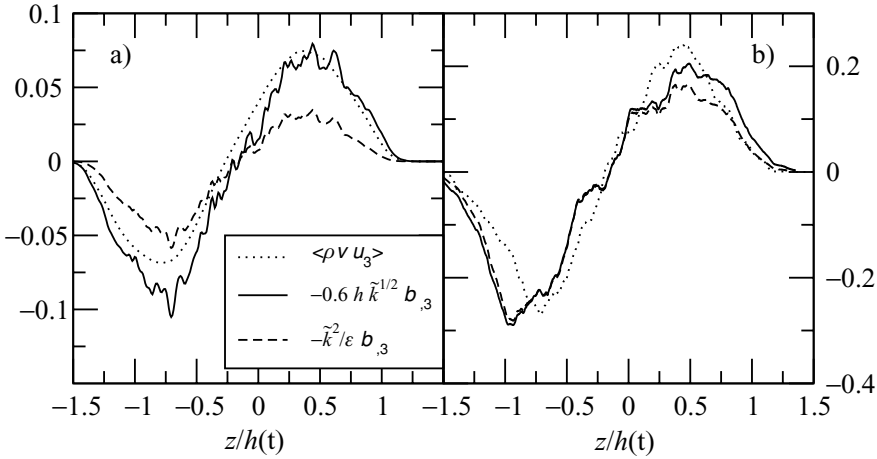


Figure 22. Comparison of $\langle \rho v u_3 \rangle$ across the layer with a gradient transport hypothesis, $0.5h\sqrt{\tilde{k}}b_{,3}$ and $-\frac{\tilde{k}^2}{\varepsilon}b_{,3}$ at (a) $t/\tau = 6$ and (b) $t/\tau = 31$. The coefficients were chosen to provide a good fit in the interior of the layer at $t/\tau = 31$.

4.4.6. Discussion

Usual turbulence eddy viscosity, $\nu'_t \sim \tilde{k}^2/\varepsilon$, does not capture the time variation of the turbulent transport in any of the equations considered, even though it provides a weak spatial fit. However, an eddy diffusivity, $\nu''_t \sim h\sqrt{\tilde{k}}$, provided a very good fit for the mass flux, both temporally and spatially, and a somewhat weaker fit for the transport terms in the mass flux, kinetic energy, and b transport equations. Unfortunately, h is a global quantity which is not available in single point turbulence models. In addition, extensions to general flows are questionable. Thus, one would like to use turbulence scales to define an eddy viscosity. The problem with the turbulent eddy diffusivity, $\nu'_t \sim \tilde{k}^2/\varepsilon$, can be traced back to the lag between the rise in the large scales energy due to buoyancy production and when this increase is felt at the viscous scales. This lag persists even long after the onset of the self-similar growth. However, since the kinetic energy and dissipation follow, to leading order, the self-similar predictions, it is conceivable that, asymptotically, the leading order terms in their self-similar expressions become dominant. In that case, ℓ and \tilde{k}^2/ε may follow the self-similar scaling with the width of the layer, h , and become useful for gradient diffusion-type closures. Nevertheless, long after the onset of the self-similar growth, the usual closures for the moment equations using the turbulence lengthscale, ℓ , and the gradient transport hypothesis for the turbulence transport or similarity arguments for the dissipation fail in RT turbulence.

5. Overview of results

The flow physics and statistics of the very large 3072^3 simulation by [1] of variable density Rayleigh–Taylor mixing layer have been studied using the single point moment equations as a diagnostic tool. There are several findings to report.

- *Mean density symmetry and mixing layer asymmetry*: the mean density profile remains symmetrical with respect to the initial condition centerline in the central region of the layer. Departures from the Boussinesq behavior (for which the layer is

symmetrical) are seen at the edges of the layer where the spike front attains speeds faster than the bubble front.

- *Non-Boussinesq effects*: the non-Boussinesq effects in the RT mixing layer manifest themselves as (1) large departure of \tilde{k} , a_3 , b from symmetry with respect to the centerline, with maxima on the light fluid side, (2) the departure of the mean pressure gradient from the hydrostatic value, (3) departure of the specific volume density correlation from the normalized density variance due to large non-Gaussian density PDF moments or large density intensity.
- *Turbulence asymmetry*: near the centerline, the mean density profile is linear. This produces a mean density fixed point at $z = 0$ and predicts that the largest mass flux is on the light fluid side. As the major production mechanisms are directly or indirectly related to the mass flux and mean density, the corresponding terms in \tilde{k} and b equations peak on the light fluid side. Thus, \tilde{k} and b are asymmetric and reach their maximum values below the centerline, on the light fluid side. For a Boussinesq fluid their maxima are on the centerline.
- *In the mass flux equation $\langle vp, i \rangle$ is one of the largest terms*: from the energy budget analysis of the a_3 equation, the specific volume pressure gradient correlation, $\langle vp, i \rangle$, is seen to be important; it is in fact the largest term in the equation. The $\langle vp, i \rangle$ term acts to reducing the rate of growth of the mass flux. This term is neglected in most single point closures for VD turbulence and will require closure for an accurate model.
- *The flow becomes self-similar relatively fast, however the lower order terms in the self-similar relations are important throughout the simulation*: the quantities examined follow, to leading order, the self-similar predictions after $t/\tau \approx 6$. While it is expected that, asymptotically, the lower order terms in the self-similar relations become negligible, throughout the simulation these terms retain their relative importance.
- *Non-equilibrium spectral cascade*: long after the onset of the self-similar growth, the transient effects in the energy spectrum remain important for the duration of the simulation. Thus, there is a time lag between the energy increase at large scales and the rise in the dissipation: the dissipation does not track the spectral energy cascade rate and this has several important consequences for the gradient transport hypothesis.
- *The eddy viscosity $\nu'_t \sim \tilde{k}^2/\varepsilon$ in the gradient transport hypothesis is in substantial error for the duration of the simulation*: using $\ell = \tilde{k}^{3/2}/\varepsilon$ as the transport lengthscale in gradient transport models leads to significant error. While the gradient transport hypothesis does capture the spatial profile of the mass flux, it does not capture its temporal variation. This is because the lengthscale, $\ell = \tilde{k}^{3/2}/\varepsilon$, based on the dissipation, is not a good approximation of the integral scale which sets the turbulent transport.
- *An eddy viscosity $\nu''_t \sim \tilde{k}^{1/2}h$ works well*: the gradient transport hypotheses in which h is the transport lengthscale and $\tilde{k}^{1/2}h$ the eddy viscosity works better in capturing both the spatial profile of the transport as well as its temporal scaling. This is true of all the second order turbulent transport terms. Unfortunately, h is an integral quantity which cannot be obtained from a single point closure.
- *Spectral anisotropy of the energy*: the turbulence structure has been examined both at large and small scales. Due to the buoyancy production anisotropy, the kinetic energy components, at the largest scales of the motion, remain anisotropic with $\approx 65\%$ of the energy in the vertical direction. Because of the cancellation between nonlinear and

viscous effects, the buoyancy force leads to a persistent anisotropy at small scales, with $\approx 50\%$ of the energy in the vertical direction at the smallest scales. In some intermediate range however, the energy is approximately isotropic.

- *The utility of Boussinesq computations:* the asymmetries in the turbulence quantities are exacerbated if the Boussinesq equations are used for the same density difference. Thus, it appears that a conservative criterion for the validity of the Boussinesq equations and a Boussinesq computation is the emergence of the asymmetries in \tilde{k} , a_3 , b .

6. Conclusions

Detailed quantitative budgets of the kinetic energy, mass flux, and density specific volume correlation transport equations together with various lengthscales and moments have been examined to (1) investigate the fluid physics in VD RT, (2) provide an archival database for validating VD turbulence models, (3) characterize and explain various asymmetries not seen in the Boussinesq case, and (4) explore the applicability of the usual turbulence scales in simple similarity type gradient transport closures.

Variable density Rayleigh–Taylor turbulence is characterized by asymmetries of the mixing layer and various turbulence quantities, not seen in the Boussinesq case. For moderate A numbers, as is the case with the 3072^3 simulation of [1] discussed here, the inner region of the mean density profile remains symmetric but develops an asymmetry at the layer edges as the bubbles and spikes fronts move with different velocities. It is the presence of a fixed point at $z = 0$ in the mean density profile, together with the departure of the mean pressure gradient from the hydrostatic pressure head, that causes the asymmetry of the turbulent kinetic energy. In addition, it was shown that the fixed point also leads to asymmetry of the normalized mass flux, a_3 , density specific volume correlation, b , and the production terms in their transport equations. All these quantities have their largest magnitude on the light fluid side.

The flow reaches a self-similar state as described by the [11] analysis, at $t/\tau = 6$, when α reaches its constant value [1]. However, all the self-similar formulae also have lower order terms which remain important throughout the simulation. Consistently, the spectral dynamics remains transient and the dissipation lags the spectral cascade rate. In addition, the turbulence lengthscale and Reynolds number do not scale as the layer width. As a result, the gradient transport hypothesis with the usual turbulent eddy diffusivity, $v'_t \sim \tilde{k}^2/\varepsilon$, and simple similarity based closures are inappropriate for this flow for the duration of the simulation. However, turbulent transport closures using a large scale eddy diffusivity, $v''_t \sim \tilde{k}^{1/2}h$, (which unfortunately is not available in a single point closure) works reasonably well.

The large scales of the flow remain anisotropic at all times due to the buoyancy production. At smaller scales, buoyancy production becomes small and in some intermediate range the flow is close to isotropic. However, in the viscous range, there is a cancellation between the viscous and nonlinear effects, so that buoyancy production retains its relative importance and there is a persistent anisotropy of the smallest scales.

In short, in VD RT turbulence: (1) Favre mean and turbulent kinetic energies, normalized mass flux, b and the production terms in their transport equations are asymmetric and have their largest magnitude on the light fluid side, (2) the flow becomes self-similar relatively fast, however, the turbulent lengthscale and Reynolds number do not scale as the layer width, (3) the gradient transport models based on the usual turbulent eddy diffusivity, $v'_t \sim \tilde{k}^2/\varepsilon$,

are not appropriate for this flow, and (4) buoyancy production changes the turbulence structure with persistent anisotropy of the smallest scales.

Acknowledgements

Computational resources at Los Alamos National Laboratory were provided through the Institutional Computing Project. This work was performed under the auspices of US Department of Energy.

References

- [1] W.H. Cabot and A.W. Cook, *Reynolds number effects on Rayleigh–Taylor instability with possible implications for type-ia supernovae*, *Nature Phys.* 2 (2006), pp. 562–568.
- [2] D. Livescu and J.R. Ristorcelli, *Variable-density mixing in buoyancy-driven turbulence*, *J. Fluid Mech.* 605 (2008), pp. 145–180.
- [3] ———, *Buoyancy-driven variable-density turbulence*, *J. Fluid Mech.* 591 (2007), pp. 43–71.
- [4] D. Besnard et al., *Turbulence transport equations for variable-density turbulence and their relationships to two field models*, Tech. Rep. LA-12303-MS, Los Alamos National Laboratory, 1992.
- [5] V. Adumitroaie, J.R. Ristorcelli, and D.B. Taulbee, *Progress in Favre–Reynolds stress closures for compressible flows*, *Phys. Fluids* 11 (1999), pp. 2696–2719.
- [6] A.W. Cook and P.E. Dimotakis, *Transition stages of Rayleigh–Taylor instability between miscible fluids*, *J. Fluid Mech.* 443 (2001), pp. 69–99, 2001.
- [7] A.W. Cook, W.H. Cabot, and P.L. Miller, *The mixing transition in Rayleigh–Taylor instability*, *J. Fluid Mech.* 511 (2004), pp. 333–362.
- [8] D.L. Youngs, *Numerical simulation of turbulent mixing by Rayleigh–Taylor instability*, *Physica D* 12 (1984), pp. 32–44.
- [9] K.I. Read, *Experimental investigation of turbulent mixing by Rayleigh–Taylor instability*, *Physica D* 12 (1984), pp. 45–58.
- [10] M.J. Andrews and D.B. Spalding, *A simple experiment to investigate two-dimensional mixing by Rayleigh–Taylor instability*, *Phys. Fluids A* 2 (1990), pp. 922–927.
- [11] J.R. Ristorcelli and T.T. Clark, *Rayleigh–Taylor turbulence: Self-similar analysis and direct numerical simulations*, LANL Report 03-4273;
J.R. Ristorcelli and T.T. Clark, *J. Fluid Mech.* 507 (2004), pp. 213–253.
- [12] G. Dimonte and M. Schneider, *Density ratio dependence of Rayleigh–Taylor mixing for sustained and impulsive acceleration histories*, *Phys. Fluids* 12 (2000), pp. 304–321.
- [13] G. Dimonte et al., *A comparative study of the turbulent Rayleigh–Taylor instability using high-resolution three-dimensional numerical simulations: The Alpha-Group Collaboration*, *Phys. Fluids* 16 (2004), pp. 1668–1692.
- [14] A. Banerjee and M.J. Andrews, *3D simulations to investigate the initial conditions effects on the growth of Rayleigh–Taylor mixing*, *Int. J. Heat Mass Transfer* (2009) in press.
- [15] S.B. Pope, *Turbulent Flows*, Cambridge University Press, Cambridge, 2000.
- [16] H. Tennekes and J.L. Lumley, *A First Course in Turbulence*, MIT Press, Cambridge, 1972.
- [17] A. Banerjee and M.J. Andrews, *Statistically steady measurements of Rayleigh–Taylor mixing in a gas channel*, *Phys. Fluids* 18 (2006), pp. 035107-1–035107-13.

Appendix 1. Homogeneous versus inhomogeneous RT turbulence

In this appendix the current variable density RT findings and those of the homogeneous RT (HRT) of [2,3] are compared. In HRT, the moment equations do not have the inhomogeneous transport terms, implying that HRT provides a simpler test case that isolates the essential nonlinearities from the inhomogeneous transport issue. The benefit is that one can more confidently use the less-expensive HRT simulations to assist with modeling the buoyancy-driven variable density hydrodynamic and mixing problems and to study initial condition dependence issues. The highest turbulent Reynolds number obtained in the HRT by [3] in a 1024^3 simulation is about 1.5 times smaller than that obtained in the 3072^3 RT discussed

here. Estimating that a 1536^3 HRT simulation is capable of getting the same Reynolds number, then there is a factor of 16 reduction in computational cost of HRT versus RT for the same Re . This estimate includes the decay phase, after the maximum \tilde{k} has been reached. If one is only interested in the transition and growth phase then one can achieve a much larger reduction in computational cost. Moreover, the statistics collected in HRT, since they are volume-averaged statistics, are more robust as compared to RT where the statistics are area averaged over planes with different Re .

In HRT, the kinetic energy increases initially due to the acceleration of the fluids, then, as the two fluids become molecularly mixed the kinetic energy decays. During this growth stage, while there is still pure fluid, HRT is very much like the RT problem in which there is always a source of pure fluid. As such, HRT is also a simpler (as well as cheaper) benchmark for understanding buoyancy effects on the turbulent motions and the subsequent mixing process.

During the growth stage of HRT, many similarities with the RT problem can be identified. The primary ones are:

- *Same potential to kinetic energy conversion process*: in both RT and HRT the rate of conversion of the potential to kinetic energy is (after the initial instant)

$$\frac{\partial}{\partial t} \mathcal{E}(z, t) \approx -g_3 \bar{\rho} a_3. \quad (56)$$

The mass flux is of central importance in the conversion of potential energy to kinetic as well as the transition and turbulence growth in both of these configurations.

- *Same mean pressure gradient*: the consequence of the HRT *ansatz* $U_3 = 0$ made in [3] in order to obtain the maximally non-equilibrium flow is that the mean pressure gradient, while constant in space, is a function of time. The mean pressure gradient is usefully represented in RT by the formula used in the HRT simulations (see Figure 10).
- *Zero Reynolds mean velocity*: moreover, $U_3 \approx 0$ in the RT configuration, as was assumed in the HRT simulations to set a free parameter in the homogeneous equations. The Favre mean velocity is not zero.
- *Equivalent L and ℓ relations*: the ratio of length-scales L/l for $A = 0.5$ reported in the HRT [3] at early times (when kinetic energy is increasing) is mirrored in the RT simulations. L is the integral scale and $\ell = \tilde{k}^{3/2}/\varepsilon$ is the turbulence lengthscale used in transport models.
- *Equivalent anisotropies*: b_{33} is the same order, perhaps a few percent larger, during the HRT kinetic energy growth stage than in RT. Values of $b_{33} \approx 0.3$ are obtained at the peak kinetic energy time.
- *Same spectral anisotropy*: the unexpected scale dependence of $b_{33}(\kappa)$ and its anisotropy in the viscous range are similar in both HRT and RT.

The only modest difference we have seen between HRT and RT is that in the growth phase HRT is more “non-equilibrium” than RT: production over dissipation ratios are much larger in HRT and higher Reynolds numbers are achieved sooner. This suggests that HRT can minimize the computational expense to generate high-Reynolds number variable density RT databases for model development as well as can be a better study for stronger “non-equilibrium” issues.